

An FFT-accelerated direct solver for electromagnetic scattering from penetrable axisymmetric objects

Jun Lai* and Michael O’Neil†

February 2, 2022

Abstract

Fast, high-accuracy algorithms for electromagnetic scattering from axisymmetric objects are of great importance when modeling physical phenomena in optics, materials science (e.g. meta-materials), and many other fields of applied science. In this paper, we develop an FFT-accelerated separation of variables solver that can be used to efficiently invert integral equation formulations of Maxwell’s equations for scattering from axisymmetric penetrable (dielectric) bodies. Using a standard variant of Müller’s integral representation of the fields, our numerical solver rapidly and directly inverts the resulting second-kind integral equation. In particular, the algorithm of this work (1) rapidly evaluates the modal Green’s functions, and their derivatives, via kernel splitting and the use of novel recursion formulas, (2) discretizes the underlying integral equation using generalized Gaussian quadratures on adaptive meshes, and (3) is applicable to geometries containing edges and points. Several numerical examples are provided to demonstrate the efficiency and accuracy of the aforementioned algorithm in various geometries.

Keywords: Electromagnetics, Müller’s integral equation, penetrable media, dielectric media, body of revolution, Fast Fourier Transform.

1 Introduction

While many scattering problems in computational electromagnetics require the solution to Maxwell’s equations in arbitrary complex geometries (e.g. radar scattering from aircraft, capacitance extraction, etc.), it is often useful to study the same scattering problems in somewhat simpler geometries, namely axisymmetric ones. This problem, of computing scattered waves in axisymmetric geometries, has a very rich history in the electrical engineering community [2, 23, 24, 45–47, 63], and recently several groups have built specialized high-order solvers for particular applications in plasma physics [54], resonance calculations [34–36], and utilizing novel integral representations [20]. Decades ago, the computation of radar cross sections and scattering phenomena in axisymmetric geometries was popular, in part, due

*School of Mathematical Sciences, Zhejiang University, Hangzhou, Zhejiang. Research was supported in part by the Funds for Creative Research Groups of NSFC (No. 11621101), the Major Research Plan of NSFC (No. 91630309), NSFC grant No. 11871427 and The Fundamental Research Funds for the Central Universities., Email: lai jun6@zju.edu.cn

†Courant Institute, New York University, New York, NY. Research was supported in part by the Office of Naval Research under award numbers #N00014-17-1-2059 and #N00014-17-1-2451. Email: oneil@cims.nyu.edu.

to the very limited computational resources available at the time: the separation of variables procedure reduced the dimension of the problem, effectively reducing the number of unknowns needed for boundary integral equation discretizations by a square-root-factor. The schemes were mostly low-order Galerkin-based (i.e. method-of-moments), and often only obtained a modest engineering precision (if accuracies were reported at all). In this work, we address the problem of scattering from homogeneous penetrable axisymmetric bodies which may contain edges, and therefore high-order adaptive discretizations of the geometry are required. Our algorithm is based on solving Müller's integral equation using a Nyström-like discretization scheme. Using modern developments in numerical analysis and quadrature, our solver is, in most cases, easily able to obtain 10-digits of accuracy using a small number of unknowns located along the boundary of a two-dimensional cross section of the scatterer. We now briefly introduce the time harmonic transmission problem for Maxwell's equations, and discuss earlier work in the field.

In regions free of electric charge and current, with electric permittivity ϵ and magnetic permeability μ , the time harmonic Maxwell's equations can be reduced to:

$$\begin{aligned}\nabla \times \mathbf{E} &= i\omega\mu\mathbf{H}, & \nabla \times \mathbf{H} &= -i\omega\epsilon\mathbf{E}, \\ \nabla \cdot \mathbf{E} &= 0, & \nabla \cdot \mathbf{H} &= 0,\end{aligned}\tag{1.1}$$

where ω denotes the angular frequency; the time dependence on the fields of $e^{-i\omega t}$ has been suppressed. It will also be useful to define the wavenumber $k = \omega\sqrt{\epsilon\mu}$. In the most general case, the material parameters are allowed to be spatially dependent tensors [38].

There are two canonical boundary value problems in classical electromagnetics, that of scattering from perfect electric conductors (PECs) and scattering in non-conducting (dielectric, or penetrable) materials with piecewise constant material properties. In this work, we will focus on the latter scattering problem. This problem, as well as the first, offers a surprising regime in which the mathematical and physics model (i.e. Maxwell's equations) is very well understood *and* agrees very closely with experimental phenomena. With this in mind, it is useful to construct numerical methods which accurately solve the underlying equations in order to complement, or partially replace, experimental design methods.

To be more precise regarding the formulation of the PDE we are focusing on, denote by Ω a closed bounded object in \mathbb{R}^3 with boundary Γ and constant material parameters ϵ_1, μ_1 . Let the background be denoted by $\Omega_0 = \mathbb{R}^3 \setminus \Omega$, also a closed region with the same boundary Γ . The background material parameters will be given by ϵ_0, μ_0 . See Figure 1. Considering Maxwell's equations (1.1) in this two-component geometry, we will assume that $\omega \geq 0$, $\epsilon_0, \mu_0 > 0$, and that

$$\begin{aligned}\Re\epsilon_1 &> 0 \text{ and } \Im\epsilon_1 \geq 0, \\ \Re\mu_1 &> 0 \text{ and } \Im\mu_1 \geq 0.\end{aligned}\tag{1.2}$$

Existence and uniqueness results for a slightly more general set of parameters, namely for those with $\Re\epsilon_1 < 0$ and $\Re\mu_1 < 0$, can be found in [59] and [50, §20]. This parameter regime covers all classical materials, as well as metamaterials with non-zero dissipation [59]. Our selection of parameters is a subset of this more general case, and therefore all existence and uniqueness results still hold.

Furthermore, many problems of considerable interest in real-world phenomena (e.g. computing radar cross sections) take the form of *scattering problems*. In this setup, the total electromagnetic field $(\mathbf{E}^{\text{tot}}, \mathbf{H}^{\text{tot}})$ is the sum of two pieces: an incident field $(\mathbf{E}^{\text{inc}}, \mathbf{H}^{\text{inc}})$ and a scattered field (\mathbf{E}, \mathbf{H}) . Both the incoming and scattered field are assumed to satisfy

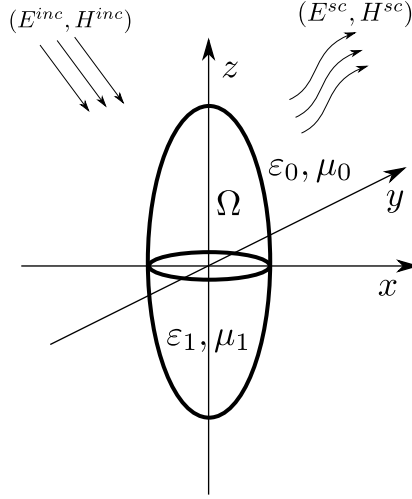


Figure 1: An axisymmetric object Ω is illuminated by a time harmonic incident wave $(\mathbf{E}^{\text{inc}}, \mathbf{H}^{\text{inc}})$. The object is penetrable with dielectric coefficients (ε_1, μ_1) . The background material is homogeneous with dielectric coefficients (ε_0, μ_0) .

Maxwell's equations, and therefore so does the total field. It is also further assumed that the scattered field (\mathbf{E}, \mathbf{H}) must satisfy the Silver-Müller radiation condition at infinity [14]:

$$\lim_{|\mathbf{x}| \rightarrow \infty} \frac{1}{|\mathbf{x}|} \left(\frac{\mathbf{x}}{|\mathbf{x}|} \times \sqrt{\varepsilon_0} \mathbf{E}(\mathbf{x}) - \sqrt{\mu_0} \mathbf{H}(\mathbf{x}) \right) = 0. \quad (1.3)$$

The physical boundary conditions along an interface between two pieces of penetrable media state that the tangential components of the total field are continuous across Γ :

$$[\mathbf{n} \times \mathbf{E}^{\text{tot}}] = 0, \quad [\mathbf{n} \times \mathbf{H}^{\text{tot}}] = 0, \quad \text{on } \Gamma. \quad (1.4)$$

Here, $[\cdot]$ denotes the jump across Γ and \mathbf{n} is the unit normal along Γ that points into the unbounded region Ω_0 . A proof of uniqueness to this boundary value problem (i.e. equations (1.1) and (1.3) with boundary condition (1.4)) with the aforementioned material parameter constraints (1.2) is given in [59], which is simpler to parse than the original treatment by Müller [50, §21, Thm 61]. We will refer to this as the Transmission Boundary Value Problem (TBVP).

Scattering from perfectly conducting bodies of revolution using integral equation methods appeared as early as 1965 [2], and we believe that the transmission boundary value problem was first directly treated in axisymmetric domains via an integral equation method (i.e. Müller's formulation) in 1966 [58]. Details of this approach, along with Fortran code, were then collected in a technical report by Mautz and Harrington in 1977 [46]. Since then, many groups in the electrical engineering community have studied scattering from bodies of revolution of various materials (e.g. from perfectly conducting metals to inhomogeneous penetrable materials). Some works addressed the issue of generating matrix elements of the decouple integral equations [23], and others focused on integral equation formulations for more complicated structures [48, 49]. Nearly all methods are based on a Galerkin discretization of the relevant boundary integral equation, frequently referred to as the boundary element method (BEM) [3] in some mathematics communities and the method of moments (MoM) [31]

in most engineering circles. There are at most a handful of works in the engineering literature which have implemented higher-order methods for these problems. Notably, a 3rd-order hybrid finite-element/boundary integral code was presented in [17] in 2006. This code still had visible errors in the monostatic radar cross section of a sphere when compared with the exact Mie-series solution [17, Fig. 3].

However, over the past decade, integral equation methods for boundary value problems in axisymmetric geometries have received a lot of attention in applied and computational mathematics, likely due to the increase in computational power (thereby enabling high-resolution experiments to be performed on a desktop or laptop) and the persistent mathematical and computational difficulties of designing high-order methods in general, complex geometries (e.g. quadrature design, geometry generation, etc.). Axisymmetric solvers based on a separation of variables approach, as in this work, provide a robust test-bed for the same integral equations which are used in general geometries, not to mention that several axisymmetric geometries are of real-world physical importance. Advances in Nyström discretization and quadrature were applied to this problem in 2004 [22], but the first recent, high-order treatments of scattering (electrostatic and acoustic) from axisymmetric objects were in 2010 [62] and 2012 [61]. Since then, various high-order accurate separation of variable methods for integral equation formulations in axisymmetric geometries have been developed for boundary value problems for Laplace’s equation, the Helmholtz equation [32, 33, 44], and more recently, Maxwell’s equations [20, 34–36] using a variety of discretization schemes, solvers, and methods for evaluating the so-called modal Green’s functions. The previous discussion is a quite complete picture of the state of integral equation-based solvers for boundary value problems in axisymmetric domains. The only work relevant to high-order methods for dielectric bodies of revolution is [36], but that work is rather terse and focused on computing eigenvalues/fields. On a related note, however, that it has been shown that high-order methods based on boundary perturbations and separation of variables (of the solution to the PDE) can be made quite efficient [10, 21, 52], and of course, high-order methods in general geometries is always a work in progress [5, 8, 9].

It is also worth mentioning some details of related work: recently, a solver for both PEC and dielectric scattering problem based on the generalized Debye source formulation [18, 19] was described in [20]. This solver, while also of high-order and stable for all frequencies (including the low-frequency limit $\omega \rightarrow 0$), is currently restricted to globally smooth geometries. The integral equation method of this paper, based on the classic one due to Müller, is also free from spurious resonances and is of Fredholm second-kind on smooth geometries (and well-conditioned on those with edges) under condition (1.2). We do not address the situation in which $\omega \rightarrow 0$. The standard integral representations based on Müller’s formulation for penetrable media include terms which are $\mathcal{O}(\omega^{-1})$, and therefore require some care in the static limit.

To summarize our contribution, the integral equation formulation and solver of this work have three main features: (1) a novel method for evaluating higher derivatives of the modal Green’s functions based on kernel splitting and recurrence relations, (2) an adaptive discretization of the generating curve based on generalized Gaussian quadratures, and (3) an integral equation formulation and discretization scheme which is compatible with geometries that contain edges. We focus our attention on Müller’s integral equation for the TBVP, but the discretization methods are applicable to integral equations arising in other fields with Green’s functions exhibiting similar singularity behavior.

The paper is organized as follows: Section 2 introduces the Müller integral representation, and its indirect form, for electromagnetic fields in piecewise constant penetrable media. Section 3 details the transformation of a surface integral equation along an axisymmetric surface into a sequence of decoupled integral equations along a curve in two dimensions using the Fourier transform in the azimuthal direction. Details of the fast kernel evaluation based on a kernel splitting technique and recursion formulas are given in Section 4. Section 5 discusses discretization of the sequence of line integrals using an adaptive mesh and generalized Gaussian quadratures for the associated weakly singular integral operators. Numerical examples are given in Section 6, including scattering results in both smooth and non-smooth geometries. Section 7 concludes the discussion with drawbacks, observations, and future research.

2 Integral equation formulations

In what follows, we will denote the exterior scattered field by $(\mathbf{E}_0, \mathbf{H}_0)$ and the interior scattered field by $(\mathbf{E}_1, \mathbf{H}_1)$. It will also be assumed that the incoming field is generated from sources exterior to Ω , i.e. in the background, and therefore inside Ω we simply have $\mathbf{E}_1 = \mathbf{E}^{\text{tot}}$ and $\mathbf{H}_1 = \mathbf{H}^{\text{tot}}$. Therefore the jump condition (1.4) along Γ can be written as

$$\begin{aligned} \mathbf{n} \times (\mathbf{E}^{\text{inc}} + \mathbf{E}_0) &= \mathbf{n} \times \mathbf{E}_1, \\ \mathbf{n} \times (\mathbf{H}^{\text{inc}} + \mathbf{H}_0) &= \mathbf{n} \times \mathbf{H}_1. \end{aligned} \quad (2.1)$$

We now turn to a derivation of the Müller's integral equation, and its indirect formulation.

2.1 The Müller integral equation

As discussed in the introduction, the goal of this paper is to design an efficient numerical solver for the time-harmonic Maxwell's equations, given in (1.1), with transmission boundary conditions (2.1) along the surface of axisymmetric objects. The same boundary value problem is also referred to as scattering from piecewise homogeneous penetrable, or dielectric, media. Using a properly formulated integral equation method automatically ensures that the scattered field obeys the radiation condition (1.3) at infinity [12, 14]. We start by defining the single-layer vector potential. Let \mathbf{J} be a vector field supported along the surface Γ . Then the single-layer potential due to \mathbf{J} is given by

$$\mathcal{S}^k \mathbf{J}(\mathbf{x}) = \int_{\Gamma} G^k(\mathbf{x}, \mathbf{y}) \mathbf{J}(\mathbf{y}) da(\mathbf{y}), \quad (2.2)$$

where it is assumed that $\mathbf{x} \notin \Gamma$ and da is the area element along Γ . Here, the function $G^k(\mathbf{x}, \mathbf{y})$ is the free space Green's function for the three dimensional Helmholtz equation:

$$G^k(\mathbf{x}, \mathbf{y}) = \frac{e^{ik|\mathbf{x}-\mathbf{y}|}}{4\pi|\mathbf{x}-\mathbf{y}|}. \quad (2.3)$$

For $\mathbf{x} \in \Gamma$, the integral operator \mathcal{S}^k is weakly-singular and continuous across Γ [14]. We now derive an integral equation for the TBVP based on what is referred to as the *direct method*. The Stratton-Chu formulation [40] provides a Green's-like reproducing formula for the incoming field in Ω using tangential traces of the fields on Γ . Let k_0 and k_1 be the wavenumbers in

the interior and exterior of Ω , respectively. Inside Ω , the incident field $(\mathbf{E}^{\text{inc}}, \mathbf{H}^{\text{inc}})$ satisfies

$$\begin{aligned} i\omega\varepsilon_0 \mathbf{E}^{\text{inc}} &= \nabla \times \nabla \times \mathcal{S}^{k_0}(\mathbf{n} \times \mathbf{H}^{\text{inc}}) - i\omega\varepsilon_0 \nabla \times \mathcal{S}^{k_0}(\mathbf{n} \times \mathbf{E}^{\text{inc}}), \\ i\omega\mu_0 \mathbf{H}^{\text{inc}} &= -\nabla \times \nabla \times \mathcal{S}^{k_0}(\mathbf{n} \times \mathbf{E}^{\text{inc}}) - i\omega\mu_0 \nabla \times \mathcal{S}^{k_0}(\mathbf{n} \times \mathbf{H}^{\text{inc}}). \end{aligned} \quad (2.4)$$

Furthermore, according to the Extinction Theorem [50], in the *interior* Ω , the exterior scattered field $(\mathbf{E}_0, \mathbf{H}_0)$ vanishes:

$$\begin{aligned} 0 &= \nabla \times \nabla \times \mathcal{S}^{k_0}(\mathbf{n} \times \mathbf{H}_0) - i\omega\varepsilon_0 \nabla \times \mathcal{S}^{k_0}(\mathbf{n} \times \mathbf{E}_0), \\ 0 &= -\nabla \times \nabla \times \mathcal{S}^{k_0}(\mathbf{n} \times \mathbf{E}_0) - i\omega\mu_0 \nabla \times \mathcal{S}^{k_0}(\mathbf{n} \times \mathbf{H}_0), \end{aligned} \quad (2.5)$$

and likewise, in the *exterior* (the background) Ω_0 , the interior scattered field $(\mathbf{E}_1, \mathbf{H}_1)$ vanishes:

$$\begin{aligned} 0 &= -\nabla \times \nabla \times \mathcal{S}^{k_1}(\mathbf{n} \times \mathbf{H}_1) + i\omega\varepsilon_1 \nabla \times \mathcal{S}^{k_1}(\mathbf{n} \times \mathbf{E}_1), \\ 0 &= \nabla \times \nabla \times \mathcal{S}^{k_1}(\mathbf{n} \times \mathbf{E}_1) + i\omega\mu_1 \nabla \times \mathcal{S}^{k_1}(\mathbf{n} \times \mathbf{H}_1). \end{aligned} \quad (2.6)$$

In order to derive an integral equation along the boundary Γ , we now let \mathbf{x} approach the boundary Γ from the interior for equations (2.4) and (2.5), and from the exterior for equation (2.6). Taking the limit of the tangential components of both sides of equations (2.4)–(2.6), where the tangential direction is defined on a parallel surface with respect to Γ [51], and using the jump property of boundary integral operators [14] and the transmission condition (2.1), we obtain the following boundary integral equation:

$$\begin{aligned} i\omega\varepsilon_0 \mathbf{n} \times \mathbf{E}^{\text{inc}} &= \frac{i\omega}{2}(\varepsilon_0 + \varepsilon_1)\mathbf{M} + (\mathcal{K}^{k_0} - \mathcal{K}^{k_1})\mathbf{J} - i\omega(\varepsilon_0\mathcal{N}^{k_0} - \varepsilon_1\mathcal{N}^{k_1})\mathbf{M}, \\ i\omega\mu_0 \mathbf{n} \times \mathbf{H}^{\text{inc}} &= \frac{i\omega}{2}(\mu_0 + \mu_1)\mathbf{J} - (\mathcal{K}^{k_0} - \mathcal{K}^{k_1})\mathbf{M} - i\omega(\mu_0\mathcal{N}^{k_0} - \mu_1\mathcal{N}^{k_1})\mathbf{J}, \end{aligned} \quad (2.7)$$

where we have set

$$\mathbf{J} = \mathbf{n} \times \mathbf{H}^{\text{tot}}, \quad \mathbf{M} = \mathbf{n} \times \mathbf{E}^{\text{tot}}, \quad (2.8)$$

and the boundary-to-boundary layer potential operators \mathcal{K}^k and \mathcal{N}^k are defined as

$$\mathcal{K}^k \mathbf{J} = \mathbf{n} \times \nabla \times \nabla \times \mathcal{S}^k \mathbf{J}, \quad (2.9)$$

$$\mathcal{N}^k \mathbf{J} = \mathbf{n} \times \nabla \times \mathcal{S}^k \mathbf{J}. \quad (2.10)$$

Both of the operators \mathcal{K}^k and \mathcal{N}^k have singular kernels; the operator \mathcal{K}^k is defined in the Hadamard finite part sense, and the operator \mathcal{N}^k is defined as a Cauchy principal value. The operator \mathcal{N}^k in (2.10) appears in the classic Magnetic Field Integral Equation (MFIE), and is in fact a weakly-singular integral operator. Integral equation (2.7) is the well-known Müller formulation for electromagnetic scattering from dielectric objects. Due to the presence of only the *difference* of hypersingular operators appearing in (2.7), note that this system of integral equations is Fredholm of the second-kind when Γ is smooth [50,55]. By the Fredholm alternative, the existence of a solution follows from the uniqueness [50,59].

When the boundary Γ is not smooth, but rather contains edges and corners, the integral operators in (2.7) are not compact, but merely bounded in the appropriate Sobolev space. In this case the proof of uniqueness is slightly more involved, but the results still hold. See [40], Theorem 5.52 for details. Our numerical examples will include geometries that are both globally smooth and merely piecewise smooth (i.e. containing edges). We see similar

high-accuracy results in both cases using the same discretization scheme (albeit with dyadic mesh-refinement near any geometric singularities).

Once equation (2.7) has been solved for the surface currents \mathbf{J} and \mathbf{M} , the exterior and interior scattered fields can be evaluated using similar Green's-like identities. For $\mathbf{x} \in \Omega_0$, we have that

$$\begin{aligned}\mathbf{E}_0 &= -\frac{1}{i\omega\varepsilon_0}\nabla \times \nabla \times \mathcal{S}^{k_0}\mathbf{J} + \nabla \times \mathcal{S}^{k_0}\mathbf{M}, \\ \mathbf{H}_0 &= \frac{1}{i\omega\mu_0}\nabla \times \nabla \times \mathcal{S}^{k_0}\mathbf{M} + \nabla \times \mathcal{S}^{k_0}\mathbf{J},\end{aligned}\tag{2.11}$$

and for $\mathbf{x} \in \Omega$, we have that

$$\begin{aligned}\mathbf{E}_1 &= \frac{1}{i\omega\varepsilon_1}\nabla \times \nabla \times \mathcal{S}^{k_1}\mathbf{J} - \nabla \times \mathcal{S}^{k_1}\mathbf{M}, \\ \mathbf{H}_1 &= -\frac{1}{i\omega\mu_1}\nabla \times \nabla \times \mathcal{S}^{k_1}\mathbf{M} - \nabla \times \mathcal{S}^{k_1}\mathbf{J}.\end{aligned}\tag{2.12}$$

2.2 An indirect formulation

Another approach that is commonly used to derive an integral equation for the TBVP is known as the *indirect method*. It is based on the fact that the pair of vector potentials $\nabla \times \mathcal{S}^k\mathbf{J}$ and $\nabla \times \nabla \times \mathcal{S}^k\mathbf{J}/ik$, set to be the electric field and magnetic field, respectively, automatically satisfy the time harmonic Maxwell equations with wavenumber k . This is sometimes referred to as the Rokhlin-Müller representation for transmission problems [50,55]; it is the generalization from electrostatics and acoustics to electromagnetics of using an indirect linear combination of a single- and double-layer potential to represent the solution. The radiation condition is also automatically satisfied via the use of these layer potentials. With this in mind, we keep the same representation for the exterior field as before in (2.11), and merely replace the appropriate dielectric constants with their interior counterparts for the interior field to write:

$$\begin{aligned}\mathbf{E}_1 &= -\frac{1}{i\omega\varepsilon_0}\nabla \times \nabla \times \mathcal{S}^{k_1}\mathbf{J} + \frac{\mu_1}{\mu_0}\nabla \times \mathcal{S}^{k_1}\mathbf{M}, \\ \mathbf{H}_1 &= \frac{1}{i\omega\mu_0}\nabla \times \nabla \times \mathcal{S}^{k_1}\mathbf{M} + \frac{\varepsilon_1}{\varepsilon_0}\nabla \times \mathcal{S}^{k_1}\mathbf{J}.\end{aligned}\tag{2.13}$$

A priori, due to the representation, these interior and exterior fields automatically satisfy Maxwell's equations. We merely need to solve for \mathbf{J} and \mathbf{M} to satisfy the transmission conditions. As before, the integral equation along Γ can be obtained by taking the limit of the tangential components of representations (2.11) and (2.13) as \mathbf{x} approaches the boundary and then forming linear combinations to enforce the transmission boundary condition. This procedure results in the integral equation:

$$\begin{aligned}i\omega\mu_0\mathbf{n} \times \mathbf{E}^{\text{inc}} &= -\frac{i\omega}{2}(\mu_1 + \mu_0)\mathbf{M} + i\omega\left(\mu_1\mathcal{N}^{k_1} - \mu_0\mathcal{N}^{k_0}\right)\mathbf{M} - \frac{\mu_0}{\varepsilon_0}\left(\mathcal{K}^{k_1} - \mathcal{K}^{k_0}\right)\mathbf{J}, \\ i\omega\varepsilon_0\mathbf{n} \times \mathbf{H}^{\text{inc}} &= -\frac{i\omega}{2}(\varepsilon_1 + \varepsilon_0)\mathbf{J} + i\omega\left(\varepsilon_1\mathcal{N}^{k_1} - \varepsilon_0\mathcal{N}^{k_0}\right)\mathbf{J} + \frac{\varepsilon_0}{\mu_0}\left(\mathcal{K}^{k_1} - \mathcal{K}^{k_0}\right)\mathbf{M}.\end{aligned}\tag{2.14}$$

This system of integral equations is an indirect form of equation (2.7) [27].

This indirect integral equation has similar properties to the classical Müller integral equation; when the boundary Γ is smooth, equation (2.14) is also Fredholm second-kind and

admits a unique solution. In the case of boundaries with edges and corners, since the integral operators in the indirect formulation are of the same order as those in the direct formulation, we have the same regularity and uniqueness results. However, note that the currents \mathbf{J} and \mathbf{M} in equation (2.14) do not represent tangential traces of the fields anymore. The advantage of this formulation is that we are able to easily construct an exact solution to the TBVP in each of the regions using the integral representations (2.11) and (2.13). This provides true verification of the accuracy of the numerical solver. In subsequent numerical experiments, we solve equation (2.14) for accuracy verification and equation (2.7) for obtaining tangential traces of the fields.

In the next section, we discuss the discretization of equation (2.7) and (2.14) along the boundaries of axisymmetric objects.

3 Fourier representation of the boundary integral operators

Discretizing integral equations in complex geometries in three dimensions to high-order is non-trivial and currently rather computationally expensive. All aspects of this problem are active areas of research: high-order geometry construction, quadrature, constructing optimal fast direct solvers, and coupling fast algorithms with quadrature methods. However, there exist many interesting applications of electromagnetic scattering from axisymmetric objects (for instance, parabolic reflectors [11], buried mines and unexploded ordnances [24], etc); in this case, variables can be separated in cylindrical coordinates resulting in a system of decoupled line integrals. The discretization and solution of integral equations along curves in two dimensions is a much easier problem, and very efficient schemes exist [29, 30, 44, 61]. The resulting Fourier decomposition scheme easily parallelizes and can address a range of rather complicated axisymmetric geometries.

A concise discussion regarding the discretization of scalar-valued integral equations along bodies of revolution is contained in [32, 61]; a modern treatment of the vector-valued case, in particular integral equation methods for Maxwell's equations, is discussed in [20, 34, 35, 54]. In each case, a choice of discretization, quadrature, and subsequent linear algebraic solver must be made. The linear systems resulting from a separation of variables integral equation approach are generally small (scaling as \sqrt{N} , where N is the number of degrees of freedom needed on the corresponding rotated surface in three dimensions) and can be rapidly solved merely using Gaussian elimination or GMRES [56] with dense matrix-vector multiplications. However, the choice of discretization and quadrature varies depending on the particular geometries of interest and the numerical tools available. For example, in [34, 35], a panel-based discretization of the geometry with exact product integration was used to find interior eigenfields by solving the Magnetic Field Integral Equation (MFIE) and the charge integral equation (ChIE). In [20, 54], the boundaries were assumed to be smooth and the resulting integral equations based on a generalized Debye formulation of electromagnetic fields [18, 19] were discretized using a trapezoidal rule along with hybrid Gauss-trapezoidal quadrature rules [1]. Neither work addressed the classic, and widely used, Müller integral equation formulation for penetrable media, which requires higher derivatives of the modal Green's functions. Furthermore, the formulation in [20] (at least in its current state) is not compatible with geometries containing edges or points; Müller's integral equation is. In what follows, we emulate the style and notation in our previous work [43] rather closely.

As in Figure 1, assume that Ω denotes an axisymmetric object (i.e. body of revolution)

with boundary Γ . The boundary will be assumed to be smooth or contain a small number of edges or points. Cylindrical coordinates will be given as (r, θ, z) , and we will denote the corresponding standard unit vectors by $(\mathbf{e}_r, \mathbf{e}_\theta, \mathbf{e}_z)$. Furthermore, we assume that the cross section of Γ in the $\theta = 0$ plane, also referred to as the generating curve γ , is parameterized counterclockwise by $\gamma(s) = (r(s), z(s))$, where s denotes arclength. This implies that the unit tangential vector along the generating curve (and Γ itself) is $\mathbf{t}(s) = r'(s) \mathbf{e}_r + z'(s) \mathbf{e}_z$, with r' and z' denoting differentiation with respect to arclength, i.e. $r' = dr/ds$. The unit exterior normal \mathbf{n} is then given by $\mathbf{n}(s) = z'(s) \mathbf{e}_r - r'(s) \mathbf{e}_z$. A surface current \mathbf{J} on Γ can be written in terms of these coordinates as $\mathbf{J} = J^1 \mathbf{t} + J^2 \mathbf{e}_\theta$. Furthermore, since Γ is always smooth in the azimuthal direction, taking the Fourier expansion of J^1 and J^2 with respect to θ yields

$$\mathbf{J}(r, z) = \sum_m \left(J_m^1(r, z) \mathbf{t} + J_m^2(r, z) \mathbf{e}_\theta \right) e^{im\theta}. \quad (3.1)$$

The dependence of the unit vectors on the variables r, θ, z will be omitted unless needed for clarity. Also, sometimes it will be useful to denote functions in terms of the arclength variable along γ , for example $J_m^1(s) = J_m^1(r(s), z(s))$.

We begin with the following lemma, which is given in [43], of which the proof is by direct computation.

Lemma 3.1 *In cylindrical coordinates, the vector potential $\mathcal{S}^k \mathbf{J}$ has the Fourier expansion*

$$\mathcal{S}^k \mathbf{J}(r_t, \theta_t, z_t) = \sum_m \left(c_m^1(r_t, z_t) \mathbf{e}_r + c_m^2(r_t, z_t) \mathbf{e}_\theta + c_m^3(r_t, z_t) \mathbf{e}_z \right) e^{im\theta_t} \quad (3.2)$$

where

$$c_m^1(r_t, z_t) = \int_\gamma J_m^1(s) r(s) r'(s) g_m^2(r_t, z_t, r(s), z(s)) ds \\ - i \int_\gamma J_m^2(s) r(s) g_m^3(r_t, z_t, r(s), z(s)) ds, \quad (3.3)$$

$$c_m^2(r_t, z_t) = i \int_\gamma J_m^1(s) r(s) r'(s) g_m^3(r_t, z_t, r(s), z(s)) ds \\ + \int_\gamma J_m^2(s) r(s) g_m^2(r_t, z_t, r(s), z(s)) ds, \quad (3.4)$$

$$c_m^3(r_t, z_t) = \int_\gamma J_m^1(s) r(s) z'(s) g_m^1(r_t, z_t, r(s), z(s)) ds, \quad (3.5)$$

and the target point is denoted as $(r_t, \theta_t, z_t) = (r(t), \theta(t), z(t))$. The kernels above are defined by

$$g_m^1(r_t, z_t, r, z) = \int_0^{2\pi} \frac{e^{ik\rho}}{4\pi\rho} e^{-im\varphi} d\varphi, \quad (3.6)$$

$$g_m^2(r_t, z_t, r, z) = \int_0^{2\pi} \frac{e^{ik\rho}}{4\pi\rho} \cos m\varphi \cos \varphi d\varphi, \quad (3.7)$$

$$g_m^3(r_t, z_t, r, z) = \int_0^{2\pi} \frac{e^{ik\rho}}{4\pi\rho} \sin m\varphi \sin \varphi d\varphi, \quad (3.8)$$

where

$$\rho = \sqrt{r_t^2 + r^2 - 2r_tr \cos \varphi + (z_t - z)^2} \quad (3.9)$$

with $\varphi = \theta_t - \theta$ and $(r, z) = (r(s), z(s))$. The functions g_m^i are commonly referred to as the modal Green's functions.

Using Lemma 3.1, we can also obtain the azimuthal Fourier decomposition of the layer potentials $\mathcal{N}^k \mathbf{J}$ and $\mathcal{K}^k \mathbf{J}$ along the boundary:

$$\begin{aligned} \mathcal{N}^k \mathbf{J}(r_t, \theta_t, z_t) = \sum_m \left(\left(\frac{\partial c_m^1}{\partial z_t} - \frac{\partial c_m^3}{\partial r_t} \right) \mathbf{t} \right. \\ \left. + \left(\frac{z'_t}{r_t} \left(c_m^2 + r_t \frac{\partial c_m^2}{\partial r_t} - im c_m^1 \right) + r'_t \left(\frac{im}{r_t} c_m^3 - \frac{\partial c_m^2}{\partial z_t} \right) \right) \mathbf{e}_\theta \right) e^{im\theta_t}, \end{aligned} \quad (3.10)$$

and by using the fact that $\mathcal{K}^k \mathbf{J} = \mathbf{n} \times (k^2 \mathcal{S}^k \mathbf{J} + \nabla \nabla \cdot \mathcal{S}^k \mathbf{J})$, where \mathcal{K}^k is given in (2.9), we have

$$\begin{aligned} \mathcal{K}^k \mathbf{J}(r_t, \theta_t, z_t) = \sum_m \left[k^2 \left(c_m^2 \mathbf{t} + (z'_t c_m^3 + r'_t c_m^1) \mathbf{e}_\theta \right) + \left(\frac{im}{r_t^2} c_m^1 + \frac{im}{r_t} \frac{\partial c_m^1}{\partial r_t} - \frac{m^2}{r_t^2} c_m^2 + \frac{im}{r_t} \frac{\partial c_m^3}{\partial z_t} \right) \mathbf{t} \right. \\ \left. + \left(z'_t \left(\frac{1}{r_t} \frac{\partial c_m^1}{\partial z_t} + \frac{\partial^2 c_m^1}{\partial z_t \partial r_t} + \frac{im}{r_t} \frac{\partial c_m^2}{\partial z_t} + \frac{\partial^2 c_m^3}{\partial z_t^2} \right) + r'_t \left(-\frac{1}{r_t^2} c_m^1 + \frac{1}{r_t} \frac{\partial c_m^1}{\partial r_t} + \frac{\partial^2 c_m^1}{\partial r_t^2} \right. \right. \right. \\ \left. \left. - \frac{im}{r_t^2} c_m^2 + \frac{im}{r_t} \frac{\partial c_m^2}{\partial r_t} + \frac{\partial^2 c_m^3}{\partial r_t \partial z_t} \right) \right) \mathbf{e}_\theta \Big] e^{im\theta_t}. \end{aligned} \quad (3.11)$$

Since this expression is valid for (r_t, z_t) along the generating curve, the gradient of γ at (r_t, z_t) is given by $\nabla \gamma(t) = (r'_t, z'_t)$.

In order to evaluate the layer potentials $\mathcal{N}^k \mathbf{J}$ and $\mathcal{K}^k \mathbf{J}$ rapidly, the values of c_m^1 , c_m^2 and c_m^3 , as well as their derivatives, need to be computed efficiently. The evaluation of the coefficients c_m^i can be performed in two steps: (1) Compute g_m^i and its derivatives, and then (2) integrate g_m^i and its derivatives (according to the above formulae for c_m^i) along the generating curve γ . There are no known numerically useful closed-form expressions for g_m^i . The evaluation of these functions occupies a significant portion of the run-time of the resulting solver [43] (approximately 50%, as shown in Table 1), and therefore an efficient scheme for computing them is important. Expansions of these functions in terms of half-order Hankel functions have, as of yet, proven to be somewhat expensive to evaluate [15], and designing robust contour integration methods for large values of m is quite complicated [28]. Furthermore, note that since g_m^i has a singularity when $z_t = z(s)$, specialized quadratures must be used when discretizing and integrating along γ . In the next two sections, we give a detailed discussion on the evaluation and integration of the modal Green's functions.

4 Fast modal kernel evaluation

Given the important role they play in solving PDEs and integral equations in axisymmetric domains, the speed of evaluating the kernel functions (3.6)-(3.8) is a very important consideration as it can affect the overall efficiency of the entire solver. Due to the existence of singularities in the free-space Green's functions, specialized routines must be developed for the evaluation of the modal Green's functions. In [43], we previously applied adaptive Gaussian quadrature to evaluate g_m^i . Although high accuracy was achieved, the algorithm was

time consuming as every matrix entry required several calls to an adaptive integration routine. In this section, we adopt an accelerated method based on recurrence relations and kernel splitting, as discussed in [20, 32, 33], and further develop an efficient evaluation procedure for computing first and second derivatives of g_m^i based on novel recurrences.

Let $(r(s), z(s))$ be replaced by (r_s, z_s) for notational simplicity. Using the fact that ρ in equation (3.9) is an even function with respect to φ on $[0, 2\pi]$, we observe that

$$g_m^2 = \frac{g_{m+1}^1 + g_{m-1}^1}{2}, \quad g_m^3 = \frac{g_{m+1}^1 - g_{m-1}^1}{2i} \quad (4.1)$$

for any mode m .

In general, unless the wave numbers of the dielectric object and background media are particularly high, only a modest number of Fourier modes m are needed for high-precision discretizations of the integral equations. Once the incoming data has been Fourier transformed along the azimuthal direction on the boundary, the number of Fourier modes needed in the discretization can be determined based on the decay of the coefficients of the data. We will denote this number, i.e. the bandwidth of the data in the azimuthal direction, by $M > 0$. Therefore, our goal is to evaluate all g_m^i for $|m| \leq M$. Furthermore, based on the relations in (4.1), we need only to evaluate g_m^1 and its derivatives efficiently; the other functions can be obtained by linear combinations.

When the target (r_t, z_t) is far away from the source (r_s, z_s) , the integral in (3.6) can be discretized using the periodic trapezoidal rule with $2M + 1$ points and therefore the fast Fourier transform (FFT) can be used to evaluate g_m^1 for $m = -M, \dots, M$. However, for (r_t, z_t) near (r_s, z_s) , the integrand is nearly singular and a prohibitively large number of discretization points would be needed to obtain sufficient quadrature accuracy. To overcome this difficulty, we adopt the kernel splitting technique, which has been successfully applied in [20, 32, 33, 61]. The main idea is to explicitly split the integrand into smooth and singular parts. Fourier coefficients of the smooths parts can be obtained numerically via the FFT, and it turns out that the coefficients of the singular part can be obtained analytically via recurrence relations. The Fourier coefficients of the original kernel can then be obtained via discrete convolution. See the previous references for thorough details, particularly [20], which provides estimates on the size of the FFT needed and other important tuning parameters.

In the following subsections, we discuss details of evaluating g_m^1 and its first and second derivatives for fixed sources and targets. Previous work on evaluating modal Green's functions has avoided second derivatives because the formulations did not involve hypersingular terms. However, the Müller formulations require the evaluation of the difference of hypersingular operators, which necessitates the following new discussion.

4.1 Evaluation of the Modal Green's Function

We begin by splitting g_m^1 into two parts:

$$\begin{aligned} g_m^1(r_t, z_t, r_s, z_s) &= \int_0^{2\pi} \frac{\cos(k\rho)}{4\pi\rho} e^{-im\varphi} d\varphi + \int_0^{2\pi} \frac{i \sin(k\rho)}{4\pi\rho} e^{-im\varphi} d\varphi \\ &= A_m^1 + A_m^2, \end{aligned} \quad (4.2)$$

where $\rho = \rho(\varphi)$, given in equation (3.9). The integrand in A_m^2 is analytic with respect to φ since the singularity is removable for $\rho = 0$. Therefore, the FFT can be applied directly to

find all A_m^2 for $-M \leq m \leq M$ at a cost of $\mathcal{O}(M \log M)$ flops. Note that special care must be taken in evaluating the kernel in A_m^2 for small values of ρ ; a truncated Taylor series about $\rho = 0$ is an easy solution.

For A_m^1 , we first consider the case $k = 0$ and denote it by \hat{q}_m . As shown in [13, 61], it holds that

$$\begin{aligned}\hat{q}_m &= \int_0^{2\pi} \frac{e^{-im\varphi}}{4\pi\rho} d\varphi \\ &= \frac{1}{4\pi} \int_0^{2\pi} \frac{\cos m\varphi}{\sqrt{r_t^2 + r_s^2 - 2r_tr_s \cos \varphi + (z_t - z_s)^2}} d\varphi \\ &= \frac{1}{2\pi\sqrt{r_tr_s}} \int_0^{2\pi} \frac{\cos m\varphi}{\sqrt{8(\chi - \cos \varphi)}} d\varphi \\ &= \frac{1}{2\pi\sqrt{r_tr_s}} \mathcal{Q}_{m-1/2}(\chi),\end{aligned}\tag{4.3}$$

where

$$\chi = \frac{r_t^2 + r_s^2 + (z_t - z_s)^2}{2r_tr_s} \geq 1\tag{4.4}$$

and $\mathcal{Q}_{m-1/2}$ is the Legendre function of the second-kind of half-degree. It can be evaluated by the following recursion formula [53]:

$$\mathcal{Q}_{m-1/2}(\chi) = 4\frac{m-1}{2m-1}\chi\mathcal{Q}_{m-3/2}(\chi) - \frac{2m-3}{2m-1}\mathcal{Q}_{m-5/2}(\chi)\tag{4.5}$$

with

$$\begin{aligned}\mathcal{Q}_{-1/2}(\chi) &= \sqrt{\frac{2}{\chi+1}} K\left(\sqrt{\frac{2}{\chi+1}}\right), \\ \mathcal{Q}_{1/2}(\chi) &= \chi\mathcal{Q}_{-1/2}(\chi) - \sqrt{2(\chi+1)} E\left(\sqrt{\frac{2}{\chi+1}}\right),\end{aligned}\tag{4.6}$$

where K and E are the complete elliptic integrals of the first and second kinds. While standard from the theory of orthogonal polynomials, we provide a derivation of the above recurrence formula in the appendix. This derivation is useful in order to obtain efficient recurrence relations for higher derivatives. Unfortunately, the recurrence formula (4.5) is unstable for increasing m , and therefore Miller's algorithm must be implemented [25]. For $\chi \approx 1$, the forward recurrence is only mildly unstable, and can be used with caveats. See [20] for an estimate on the number of terms that can be evaluated accurately in this regime.

In order to evaluate g_m^1 for $k \neq 0$, we apply the convolution technique proposed in [61] with a slight modification. Note that A_m^1 is merely the Fourier transform of a product of functions, which can be computed as a discrete convolution:

$$\begin{aligned}A_m^1 &= \int_0^{2\pi} f(\varphi) q(\varphi) e^{-im\varphi} d\varphi \\ &= \frac{1}{2\pi} \sum_{n=-\infty}^{\infty} \hat{f}_n \hat{q}_{m-n},\end{aligned}\tag{4.7}$$

where

$$f(\varphi) = \cos(k\rho(\varphi)), \quad q(\varphi) = \frac{1}{4\pi\rho(\varphi)}\tag{4.8}$$

and \hat{f}_m denotes the m th Fourier series coefficient of the function f :

$$\hat{f}_m = \int_0^{2\pi} f(\varphi) e^{-im\varphi} d\varphi. \quad (4.9)$$

The representation of A_m^1 in (4.7) is a discrete convolution with infinite extent, which is impractical for numerical purposes. However, since $f = \cos k\rho$ is an analytic function of φ , its Fourier series converges rapidly. Therefore, the above convolution can be truncated:

$$A_m^1 = \frac{1}{2\pi} \sum_{n=-N}^N \hat{f}_n \hat{q}_{m-n}, \quad (4.10)$$

where N is chosen such that $|\hat{f}_n| \leq \epsilon$ for some user-specified precision $\epsilon > 0$. As is well known [7], discrete convolutions can be computed efficiently using the FFT and properties of the discrete Fourier transform (DFT). To begin with, denote by $\hat{\mathbf{f}}$ the vector of Fourier coefficients \hat{f}_n , by $\hat{\mathbf{q}}$ the vector of Fourier coefficients \hat{q}_n , and by \mathbf{A}^1 the vector with elements A_{-N}^1, \dots, A_N^1 . Letting \mathbf{D} denote the $(2N+1) \times (2N+1)$ DFT matrix, we have:

$$\begin{aligned} \mathbf{A}^1 &= \mathbf{D}^{-1} \mathbf{D} \mathbf{A}^1 \\ &= \mathbf{D}^{-1} \mathbf{D} (\hat{\mathbf{f}} * \hat{\mathbf{q}}) \\ &= \mathbf{D}^{-1} (\mathbf{D} \hat{\mathbf{f}} \odot \mathbf{D} \hat{\mathbf{q}}) \\ &= \mathbf{D}^{-1} (\mathbf{D}^2 \mathbf{f} \odot \mathbf{D} \hat{\mathbf{q}}) \\ &= \mathbf{D}^{-1} (\mathbf{f} \odot \mathbf{D} \hat{\mathbf{q}}) \end{aligned} \quad (4.11)$$

where $*$ denotes the cyclic convolution, \odot denotes the pointwise Hadamard product of two vectors, and \mathbf{f} denotes the vector obtained from a $2N+1$ -point equispaced sampling of the functions f on the interval $[0, 2\pi)$. The last identity follows from the fact that f is an even function. Note that a larger extent of coefficients \hat{q}_n will be needed than for \hat{f}_n due to the definition of the convolution; denote this bandwidth as M_q . Due to the fact that the coefficients \hat{f}_n decay rapidly, this sequence can be zero-padded easily (and recall that \hat{q}_n is obtained analytically). In practice, the bandlimit M_q can be determined based on the desired number of coefficients A_m^1 and subsequently all FFTs are of size $2M_q + 1$, with \mathbf{f} being computed from a $(2M_q + 1)$ -equispaced sampling of f on $[0, 2\pi)$.

4.2 Evaluation of the first derivatives

Let us now focus on the derivative of g_1^m with respect to r_t , as the evaluation of the derivative with respect to z_t is similar. The derivative with respect to r_t is given as

$$\frac{\partial g_m^1}{\partial r_t} = \frac{1}{4\pi} \int_0^{2\pi} \frac{(ik\rho e^{ik\rho} - e^{ik\rho}) r_d}{\rho^3} e^{-im\varphi} d\varphi, \quad (4.12)$$

where $r_d = r_t - r_s \cos \varphi$. Splitting the kernel on the right hand side of (4.12) into smooth and singular parts leads to

$$\begin{aligned} \frac{\partial g_m^1}{\partial r_t} &= \frac{1}{4\pi} \int_0^{2\pi} \frac{i(k\rho \cos(k\rho) - \sin(k\rho)) r_d}{\rho^3} e^{-im\varphi} d\varphi \\ &\quad - \frac{1}{4\pi} \int_0^{2\pi} \frac{-k \sin(k\rho) r_d}{\rho} e^{-im\varphi} d\varphi - \frac{1}{4\pi} \int_0^{2\pi} \frac{\cos(k\rho) r_d}{\rho^3} e^{-im\varphi} d\varphi \\ &= B_m^1 + B_m^2 + B_m^3, \end{aligned} \quad (4.13)$$

where $\rho = \rho(\varphi)$ as before. By Taylor expansion, one can easily see that the integrands in B_m^1 and B_m^2 are analytic with respect to φ due to the removable singularities. Therefore, once again a modestly-sized FFT is an efficient mean to evaluate B_m^1 and B_m^2 . For B_m^3 , we again consider the case when $k = 0$ and $r_d = 1$, which is denoted by \hat{p}_m ,

$$\begin{aligned}
\hat{p}_m &= \frac{1}{4\pi} \int_0^{2\pi} \frac{1}{\rho^3} e^{-im\varphi} d\varphi \\
&= \frac{1}{4\pi} \int_0^{2\pi} \frac{\cos m\varphi}{(r_t^2 + r_s^2 - 2r_t r_s \cos \varphi + (z_t - z_s)^2)^{3/2}} d\varphi \\
&= \frac{1}{4\pi(2r_t r_s)^{3/2}} \int_0^{2\pi} \frac{\cos m\varphi}{(\chi - \cos \varphi)^{3/2}} d\varphi \\
&= \frac{1}{4\pi(2r_t r_s)^{3/2}} \mathcal{S}_m(\chi).
\end{aligned} \tag{4.14}$$

It can be shown the function \mathcal{S}_m is related to the functions $\mathcal{Q}_{m-1/2}$ and $\mathcal{Q}_{m-3/2}$. The following relationship holds for $m \geq 1$:

$$\mathcal{S}_m(\chi) = \sqrt{8} \frac{(1-2m)\chi \mathcal{Q}_{m-1/2}(\chi) - (1-2m) \mathcal{Q}_{m-3/2}(\chi)}{\chi^2 - 1}. \tag{4.15}$$

A proof of the above formula is contained in Appendix A. The sequence \hat{p}_m can easily be obtained once the values $\mathcal{Q}_{m-1/2}(\chi)$ have been computed. With p_m available, the sequence of B_m^3 can be obtained via a convolution technique similar to the evaluation of A_m^1 . A nearly identical procedure can be carried out to compute $\partial g_m^1 / \partial z_t$.

4.3 Evaluation of the second derivatives

The procedure for evaluating the second partial derivatives of g_m^1 is similar to that of evaluating the first partial derivatives, as detailed in the previous section. As before, only the evaluation of $\partial^2 g_m^1 / \partial r_t^2$ will be discussed since the evaluation of $\partial^2 g_m^1 / \partial z_t^2$ and $\partial^2 g_m^1 / \partial z_t \partial r_t$ are very similar. Taking the second derivative of g_m^1 with respect to r_t we have,

$$\begin{aligned}
\frac{\partial^2 g_m^1}{\partial r_t^2} &= \frac{1}{4\pi} \int_0^{2\pi} \left(\left(ik \frac{ik\rho e^{ik\rho} - e^{ik\rho}}{\rho^2} - \frac{ik\rho^2 e^{ik\rho} - 2e^{ik\rho}}{\rho^3} \right) \cdot \frac{r_d^2}{\rho^2} \right. \\
&\quad \left. + \frac{ik\rho e^{ik\rho} - e^{ik\rho}}{\rho^2} \cdot \left(\frac{1}{\rho} - \frac{r_d^2}{\rho^3} \right) \right) e^{-im\varphi} d\varphi, \tag{4.16}
\end{aligned}$$

where, as before, $r_d = r_t - r_s \cos \varphi$. In order to apply the kernel splitting technique, we now decompose the right hand side in the above formula into the sum of six terms, listed according to the order of the singularities in their integrands:

$$\frac{\partial^2 g_m^1}{\partial r_t^2} = C_m^1 + C_m^2 + C_m^3 + C_m^4 + C_m^5 + C_m^6 \tag{4.17}$$

with

$$\begin{aligned}
C_m^1 &= \frac{1}{4\pi} \int_0^{2\pi} \frac{ik\rho \cos k\rho - i \sin k\rho}{\rho^3} e^{-im\varphi} d\varphi, \\
C_m^2 &= -\frac{1}{4\pi} \int_0^{2\pi} \frac{k \sin k\rho}{\rho} \cdot \frac{1}{\rho} e^{-im\varphi} d\varphi, \\
C_m^3 &= -\frac{1}{4\pi} \int_0^{2\pi} \frac{ik^2 \sin(k\rho)}{\rho} \cdot \frac{r_d^2}{\rho^2} e^{-im\varphi} d\varphi, \\
C_m^4 &= -\frac{1}{4\pi} \int_0^{2\pi} \left(k^2 \cos(k\rho) + 3 \left(\frac{-k\rho \sin k\rho}{\rho^2} + \frac{ik \cos k\rho - i \sin k\rho}{\rho} \right) \right) \frac{r_d^2}{\rho^3} e^{-im\varphi} d\varphi, \\
C_m^5 &= -\frac{1}{4\pi} \int_0^{2\pi} \frac{\cos k\rho}{\rho^3} e^{-im\varphi} d\varphi, \\
C_m^6 &= \frac{1}{4\pi} \int_0^{2\pi} \frac{(\cos k\rho) r_d^2}{\rho^5} e^{-im\varphi} d\varphi.
\end{aligned} \tag{4.18}$$

Examining each term closely, we have that:

- By Taylor series expansion the integrand in C_m^1 is analytic. It can therefore be evaluated via the trapezoidal rule.
- To evaluate C_m^2 , since the singularity in the integrand is $1/\rho$, we can apply the same method as evaluating A_m^1 in Section 4.1.
- The singular part of the integrand of C_m^3 is $1/\rho^2$. Consider the Fourier transform of $1/\rho^2$ with respect to φ , which we denote by \hat{h}_m :

$$\begin{aligned}
\hat{h}_m &= \frac{1}{4\pi} \int_0^{2\pi} \frac{e^{-im\varphi}}{\rho^2} d\varphi \\
&= \frac{1}{4\pi} \int_0^{2\pi} \frac{\cos m\varphi}{r_t^2 + r_s^2 - 2r_t r_s \cos \varphi + (z_t - z_s)^2} d\varphi \\
&= \frac{1}{8\pi r_t r_s} \int_0^{2\pi} \frac{\cos m\varphi}{(\chi - \cos \varphi)} d\varphi \\
&= \frac{1}{\pi r_t r_s} \mathcal{T}_m(\chi),
\end{aligned} \tag{4.19}$$

where \mathcal{T}_m satisfies the following recursion formula for $m \geq 1$ (proof given in Appendix A):

$$\mathcal{T}_{m+1}(\chi) = 2\chi \mathcal{T}_m(\chi) - \mathcal{T}_{m-1}(\chi). \tag{4.20}$$

Notably, this is the same recurrence relation as for Chebychev polynomials, but with different initial values:

$$\mathcal{T}_0(\chi) = \frac{2\pi}{\sqrt{\chi^2 - 1}}, \tag{4.21}$$

$$\mathcal{T}_1(\chi) = -2\pi + \chi \mathcal{T}_0(\chi). \tag{4.22}$$

- The singularity in the integrand of C_m^4 is $1/\rho^3$, and it can be evaluated following the discussion regarding the computation of B_m^3 in Section 4.2.

- For C_m^5 and C_m^6 , their singular terms are $1/\rho^3$ and $1/\rho^5$, respectively. Although there are no essential difficulties in evaluating them using the same kernel splitting technique, note that they will eventually be used when evaluating the second derivative of c_m^i in equations (3.3)–(3.5). This requires the evaluation of hypersingular kernels. However, this numerical difficulty can be avoided by observing that only the difference of C_m^5 and C_m^6 (with different wavenumbers k_0 and k_1) appear in the integral equations (2.7) and (2.14). The order of the singularity in evaluating C_m^5 or C_m^6 can therefore be reduced by instead directly evaluating the difference kernel. Denote by C_m^{5,k_i} and C_m^{6,k_i} the dependence on wavenumber k_i , for $i = 0, 1$. By direct computation, we have:

$$\begin{aligned} C_m^{5,k_0} - C_m^{5,k_1} &= -\frac{1}{4\pi} \int_0^{2\pi} \left(\frac{\cos k_0 \rho - \cos k_1 \rho}{\rho^2} \right) \frac{1}{\rho} e^{-im\varphi} d\varphi \\ C_m^{6,k_0} - C_m^{6,k_1} &= \frac{1}{4\pi} \int_0^{2\pi} \left(\frac{\cos k_0 \rho - \cos k_1 \rho}{\rho^2} \right) \frac{r_d^2}{\rho^3} e^{-im\varphi} d\varphi. \end{aligned} \quad (4.23)$$

Therefore, the singularities in the integrand of the differences of C_m^{5,k_i} or C_m^{6,k_i} are $1/\rho$ and $1/\rho^3$, respectively. Their evaluation follows the same procedure as evaluating A_m^1 and B_m^3 . Once all the values of C_m^i have been obtained, the evaluation of $\partial^2 g_m^1 / \partial r_1^2$ is obtained via the summation in (4.17).

Lastly, it is worth pointing out that for a fixed target r_t, z_t and source r_s, z_s the evaluation of \hat{q}_m, \hat{p}_m and \hat{h}_m in equations (4.3), (4.14) and (4.19) dominate the cost of kernel evaluation. However, these values can be reused during the computation of the value of g_m^1 and its derivatives. This offers a significant savings in the cost of kernel evaluation.

5 Generalized Gaussian Quadrature

Once a scheme is in place to evaluate the modal Green's functions and their derivatives, the next step is to discretize each decoupled modal integral equation along the generating curve γ . We use a Nyström-like method for discretizing the integral equations. Since the modal Green's functions have logarithmic singularities [13, 15], any efficient Nyström-like scheme will require a quadrature that accurately evaluates weakly-singular integral operators. For high-accuracy integration, one can construct the quadrature based on the kernel splitting technique as in [41]. However, this will become tedious given the many formulas for the singularities in the derivatives of g_m^i . For our numerical simulations, we implemented a panel-based discretization scheme using generalized Gaussian quadratures to evaluate the layer potentials. See [6, 29] for an in-depth discussion of generalized Gaussian quadrature schemes. The panel-based discretization scheme of this paper, as opposed to that based on hybrid-Gauss trapezoidal rules [1], as presented in [20, 54], allow for adaptive discretizations, in particular, axisymmetric surfaces in three dimensions with edges and points.

To this end, we describe the procedure in general for any weakly-singular integral operator with logarithmically-singular kernel g . For a smooth function ψ , the goal is to evaluate, with high-order accuracy, the integral

$$\mathcal{S}\psi(\mathbf{x}) = \int_{\gamma} g(\mathbf{x}, \mathbf{y}) \psi(\mathbf{y}) ds(\mathbf{y}), \quad (5.1)$$

where \mathbf{x} and \mathbf{y} denote *targets* and *sources* on the generating curve $\gamma \subset \mathbb{R}^2$. As before, assume that the generating curve γ is parameterized as $\gamma(s)$, where s is arclength. The total

arclength will be denoted by L . The parameter domain $[0, L]$ is first divided into N panels. This division can be either uniform or nonuniform, depending on the particular geometry. Each of the corresponding N image panels $\gamma_i \subset \gamma$, and therefore any function supported on it, is discretized using p scaled Gauss-Legendre nodes. In a true Nyström discretization scheme, the integral in (5.1) would be approximated as

$$\mathcal{S}\psi(\mathbf{x}_{ln}) \approx \sum_{i=1}^N \sum_{j=1}^p w_{lnij} g(\mathbf{x}_{ln}, \mathbf{x}_{ij}) \psi(\mathbf{x}_{ij}), \quad (5.2)$$

where \mathbf{x}_{ln} is the n th Gauss-Legendre node on panel l , \mathbf{x}_{ij} is the j th Gauss-Legendre node on panel i , and w_{lnij} is the Nyström quadrature weight for this term. However, it is generally numerically difficult to derive efficient, high-accuracy Nyström schemes in which the quadrature nodes are the same as the discretization nodes (i.e. the points at which ψ are sampled, the p Gauss-Legendre nodes on each panel). Often it can be very beneficial to use additional (or at least different) quadrature *support nodes* for approximating the integral. In general, we instead approximate the layer potential $\mathcal{S}\psi$ in (5.1) by

$$\mathcal{S}\psi(\mathbf{x}_{ln}) \approx \sum_{i=1}^N \sum_{j=1}^p Q(\mathbf{x}_{ln}, \mathbf{x}_{ij}) \psi(\mathbf{x}_{ij}), \quad (5.3)$$

where Q is referred to as the *quadrature kernel*. For non-adjacent panels (i.e. when the source and target are well separated), we simply set $Q(\mathbf{x}_{ln}, \mathbf{x}_{ij}) = w_{ij} g(\mathbf{x}_{ln}, \mathbf{x}_{ij})$, where w_{ij} is the standard j th scaled Gauss-Legendre weight on panel i . Therefore, for non-adjacent panels, the order of convergence is expected to be $2p - 1$, although rigorous analysis and estimates on the number of digits obtained requires knowledge of the regularity of the density function ψ .

On the other hand, along adjacent panels and self-interaction panels, a pre-computed generalized Gaussian quadrature is applied [6]. More specifically, to compute the integral over panel γ_i at a target \mathbf{x}_{ln} on the same (or adjacent) panel, we approximate $\mathcal{S}\psi(\mathbf{x}_{ln})$ as

$$\begin{aligned} \mathcal{S}\psi(\mathbf{x}_{ln}) &= \int_{\gamma_i} g(\mathbf{x}_{ln}, \mathbf{y}) \psi(\mathbf{y}) ds(\mathbf{y}) \\ &\approx \sum_{j=1}^p c_{ij} \int_{\gamma_i} g(\mathbf{x}_{ln}, \mathbf{y}) P_j^i(\mathbf{y}) ds(\mathbf{y}) \\ &= \sum_{j=1}^p c_{ij} I_j(\mathbf{x}_{ln}), \end{aligned} \quad (5.4)$$

where P_j^i is the scaled Legendre polynomial of degree $j - 1$ on panel γ_i , the numbers c_{ij} are the Legendre expansion coefficients of the degree $j - 1$ interpolating polynomial for ψ , and $I_j(\mathbf{x}_{ln})$ is merely a number, given by:

$$I_j(\mathbf{x}_{ln}) = \int_{\gamma_i} g(\mathbf{x}_{ln}, \mathbf{y}) P_j^i(\mathbf{y}) ds(\mathbf{y}). \quad (5.5)$$

For a fixed \mathbf{x}_{ln} , each $I_j(\mathbf{x}_{ln})$ contains no unknowns and can be evaluated via a pre-computed high-accuracy generalized Gaussian quadrature. The number of nodes required in these quadratures may vary, and details regarding the construction of these quadratures via a non-linear optimization procedure are discussed in [6]. An analogous Nyström-like discretization

scheme along surfaces in three dimensions is discussed in [5]. Fortran code for computing these generalized Gaussian quadrature rules is available at github.com/JamesCBremerJr/GGQ. In our numerical examples, we use 16th-order generalized Gaussian rules which contain 16 support nodes and weights for self-interacting panels (which vary according to the location of the target) and 48 support nodes and weights on adjacent panels (which are target independent).

Remark 1 *We would like to point out that this type of quadrature, generalized Gaussian quadratures, often do not exhibit convergence in the classical sense; similar to classical Gaussian quadratures for polynomials, they are accurate to machine precision when applied to a fixed set of functions. When discretizing to high-order, often machine precision (or maximum precision, up to conditioning) is obtained before any convergence study can be carried out (unless extended precision calculations are used). In our case, for example, the k th-order quadratures for self-interacting panels are exact for integrals of the form*

$$I(x) = \int_{-1}^1 (p(y) \log |x - y| + q(y)) dy,$$

where $x \in (-1, 1)$ is a root of the k th-degree Legendre polynomial and p, q are any polynomials of degree less than k . See [6, 60] for a discussion regarding the construction of these quadratures.

Continuing, note that each c_{ij} can be obtained via application of a $p \times p$ transform matrix acting on values of ψ . Denote this transform matrix as \mathbf{U}^i , and its entries as U_{jk}^i . Inserting this into (5.4), we have

$$\begin{aligned} \mathcal{S}\psi(\mathbf{x}_{ln}) &\approx \sum_{j=1}^p c_{ij} I_j(\mathbf{x}_{ln}) \\ &= \sum_{j=1}^p \sum_{k=1}^p U_{jk}^i \psi(\mathbf{x}_{ik}) I_j(\mathbf{x}_{ln}) \\ &= \sum_{k=1}^p \left(\sum_{j=1}^p U_{jk}^i I_j(\mathbf{x}_{ln}) \right) \psi(\mathbf{x}_{ik}) \\ &= \sum_{k=1}^p Q(\mathbf{x}_{ln}, \mathbf{x}_{ik}) \psi(\mathbf{x}_{ik}). \end{aligned} \tag{5.6}$$

The above formula provides the expression for the quadrature kernel Q in this case.

In the case that γ is only piecewise smooth, a graded mesh near the corners is used to maintain high accuracy. After uniform discretization of each smooth component of γ , we perform a dyadic refinement on panels that impinge on each corner point. Unless *very* specialized quadrature and discretization schemes are used [57], adaptive refinement is needed in geometries with edges and corners in order to resolve both the numerical evaluation of the integral operator as well as to resolve the solution to the integral equation. Integral operators with logarithmic singularities cease to be compact on Lipschitz domains, but are still bounded operators on $L^2 \rightarrow L^2$ [4, 16]. Dyadic refinement is therefore an appropriate discretization scheme to approximate these integrals and functions. We then apply the p th-order generalized Gaussian quadrature on each of the refined panels. This procedure, along with proper quadrature weighting, has been shown to obtain very high accuracy results [4].

6 Numerical Examples

In this section, we apply the discretization and quadrature technique of the previous section to the separation of variables formulation of Müller's integral equation to compute electromagnetic scattering from various penetrable axisymmetric objects. In order to verify the accuracy of the solver, we choose to test the extinction theorem by solving the indirect Müller formulation (2.14) with an artificial solution. Specifically, we define the field in Ω to be generated by a current loop located in Ω_0 :

$$\begin{aligned} \mathbf{E}_1 &= \nabla \times \int_{\ell} G^{k_1}(\cdot, \mathbf{y}) d\mathbf{l}(\mathbf{y}), \\ \mathbf{H}_1 &= \frac{1}{i\omega\mu_1} \nabla \times \nabla \times \int_{\ell} G^{k_1}(\cdot, \mathbf{y}) d\mathbf{l}(\mathbf{y}), \end{aligned} \quad (6.1)$$

where ℓ is a small loop centered at (x_0, y_0, z_0) and located in the plane $z = z_0$. Throughout all the numerical examples, we let the center of the loop ℓ be $(0.4, 0.5, 5.0)$ with radius 0.42. The field in Ω_0 is simply set to be zero, i.e. $\mathbf{E}_0 = 0$, $\mathbf{H}_0 = 0$. These known fields are used to generate the boundary data for the TBVP. Since both fields satisfy Maxwell equations in Ω and Ω_0 with wavenumber k_1 and k_0 , respectively, by uniqueness, solving equation (2.14) will result in functions \mathbf{J} and \mathbf{M} that can be used to reconstruct the known fields.

To compute tangential field traces from an actual scattering problem, we solve Müller's formulation (2.7) with an incident plane wave:

$$\begin{aligned} \mathbf{E}^{\text{inc}}(\mathbf{x}) &= (\mathbf{d} \times \mathbf{p}) \times \mathbf{d} \exp(ik_0 \mathbf{d} \cdot \mathbf{x}), \\ \mathbf{H}^{\text{inc}}(\mathbf{x}) &= \mathbf{d} \times \mathbf{p} \exp(ik_0 \mathbf{d} \cdot \mathbf{x}), \end{aligned} \quad (6.2)$$

where \mathbf{d} is the propagation direction and $\mathbf{d} \times \mathbf{p}$ is an orthogonal polarization vector; both are unit vectors [39]. Unless specifically given, throughout all the examples, we let

$$\begin{aligned} \mathbf{d} &= (\cos \theta_1 \sin \varphi_1, \sin \theta_1 \sin \varphi_1, \cos \varphi_1), \\ \mathbf{p} &= (\cos \theta_2 \sin \varphi_2, \sin \theta_2 \sin \varphi_2, \cos \varphi_2), \end{aligned} \quad (6.3)$$

with $\theta_1 = \pi/3$, $\varphi_1 = 2\pi/3$, $\theta_2 = \pi/2$, and $\varphi_2 = \pi/3$. The far field pattern of the scattered wave can be found by letting $|\mathbf{x}| \rightarrow \infty$ in (2.11) and using the asymptotic form of the Green's function (2.3):

$$\begin{aligned} |\mathbf{E}_{\infty}(\theta, \varphi)| &= \frac{1}{4\pi} \left| \frac{1}{i\omega\epsilon_0} \left(k_0^2 \int_{\Gamma} e^{-ik_0 \mathbf{x} \cdot \mathbf{y}} \mathbf{J}(\mathbf{y}) ds(\mathbf{y}) \right. \right. \\ &\quad \left. \left. - \int_{\Gamma} \nabla_{\mathbf{y}} e^{-ik_0 \mathbf{x} \cdot \mathbf{y}} \nabla_{\Gamma} \cdot \mathbf{J}(\mathbf{y}) ds(\mathbf{y}) \right) + \int_{\Gamma} \nabla_{\mathbf{y}} e^{-ik_0 \mathbf{x} \cdot \mathbf{y}} \times \mathbf{J}(\mathbf{y}) ds(\mathbf{y}) \right|, \end{aligned} \quad (6.4)$$

where $\theta \in [0, 2\pi]$ is the azimuthal angle, $\varphi \in [0, \pi]$ is the angle with respect to the positive z axis, and $\mathbf{x} = (\cos \theta \sin \varphi, \sin \theta \sin \varphi, \cos \varphi)$ is a point on the unit sphere. The gradient operator with respect to \mathbf{y} is denoted $\nabla_{\mathbf{y}}$, and ∇_{Γ} is the surface divergence operator along Γ . The norm of \mathbf{H}_{∞} is the same as that of \mathbf{E}_{∞} .

The accuracy that controls the kernel evaluation (i.e. where to truncate Fourier coefficients in the discrete convolutions) and the number of Fourier modes in the decomposition of the incident wave is set to be 10^{-12} . We apply the 16th-order Nyström-like discretization described earlier in Section 5 to each modal integral equation along the generating curve. All

experiments were implemented in FORTRAN 90 and carried out on an HP workstation with twenty 2.7Ghz Intel cores and 128Gb of RAM. We made use of OPENMP for parallelism across decoupled Fourier modes; linear systems were solved via **LU**-factorization using a standard LAPACK library and the code was compiled using the GCC FORTRAN compiler. Various fast direct solvers such as [26, 37, 42, 44] could be applied if larger problems were involved, but our examples did not warrant such methods.

Remark 2 *Most of the following numerical experiments show accuracies of approximately 10^{-10} in relative precision. This is to be expected: the modal Green's functions are computed to 12 digits of relative accuracy (as mentioned above), and the data is resolved to an L^2 norm of 10^{-12} . The remaining loss of precision arise from the inherent condition number of the problem, which remains very small at modestly sized frequencies because of the second-kind integral equation formulation. In addition, we apply L^2 weighting, as described in [4], to the matrix elements in order to handle any non-physical ill-conditioning due to dyadic refinement along the generating curve. When $k_0 = 10$ and $k_1 = 5$, the approximate condition number of the 0th-mode system matrices for examples with smooth geometries in Section 6.1 and 6.2 is $4.93E3$. The approximate condition number of the 0th-mode system matrix in Section 6.3 is $1.35E3$ and in Section 6.4 is $1.43E4$ (obtained by the function `ZGESVX` in LAPACK).*

Remark 3 *It is generally difficult to analytically parameterize the generating curve with respect to arclength. In the following examples, instead of resampling the curve to obtain an arclength discretization, the generating curve is sampled at Legendre nodes in some parameter t , not necessarily arclength. Any previous formulae based on an arclength parameterization can be easily adjusted with factors of ds/dt to account for the change of variables.*

Remark 4 *The examples we tested here are all for the scattering of a single object. The algorithm, however, can be extended to the scattering of multiple axisymmetric objects by transforming the incident field into the local coordinate of each object [27, 29]. This will be considered in future work.*

We make use of the following notation in the subsequent tables that present data from our scattering experiments:

- k_0 : the exterior wavenumber,
- k_1 : the interior wavenumber,
- N_f : the number of Fourier modes in the azimuthal direction used to resolve the solution. In other words, the Fourier modes are $-N_f, -N_f + 1, \dots, N_f - 1, N_f$.
- N_{pts} : the total number of points used to discretize γ ,
- T_{kernel} : the time (seconds) to evaluate all the relevant modal Green's functions,
- T_{matgen} : the time (seconds) to construct the relevant matrix entries for all integral equations,
- T_{solve} : the time (seconds) to solve the linear system by **LU**-factorization for all modes,
- T_{add} : the time (seconds) to solve with an additional right-hand side once the matrix is factorized,

- E_{error} : the relative ℓ^2 error of the electric and magnetic fields measured at a few points randomly placed inside Ω .

6.1 Example 1: Scattering from a Torus

Consider a torus with the generating curve given by

$$\begin{aligned} r(t) &= 2 + \cos(t), \\ z(t) &= 0.5 \sin(t), \end{aligned} \tag{6.5}$$

for $t \in [0, 2\pi)$. The accuracy of the integral equation solver was tested in this geometry using the extinction theorem (described above in Section 6) with known boundary data and fields given in equation (6.1). The accuracy of the solver was verified at several wavenumbers, and results are shown in Table 1a. Using around 25 points per wavelength, approximately 8 digits of relative accuracy in the fields were obtained for most of the cases. Note that the CPU time is dominated by the formation of the system matrix, which (as expected) roughly scales quadratically with the number of unknowns. For the same number of unknowns, the computational time depends linearly on the number of Fourier modes. Although the linear systems are decoupled across modes (this makes parallelization straightforward), we present the computational time T_{solve} in Table 1a as the total matrix inversion time via sequential solve. Despite its $\mathcal{O}(N_f N_{pts}^3)$ complexity, it is still much smaller than T_{matgen} . Once the matrix is factorized, additional solves for new right hand sides are very fast.

For an incident plane wave, given in equation (6.2), Figure 2 shows the real part of the x -component of the electric current \mathbf{J} , which is $\Re(\mathbf{n} \times \mathbf{H}^{\text{tot}})_x$ by (2.8), and the far field pattern at $\varphi = \frac{\pi}{2}$ and $\theta = 0$, respectively. The exterior wavenumber is set to be $k_0 = 10.0$ and the interior is set to be $k_1 = 5.0$. When $\varphi = \pi/2$, we see a maximum at $\theta = \pi/3$ and a minimum near $\theta = 4\pi/3$. This is due to specular reflection.

Since the exact solution to the true scattering problem is not known, in order to verify the accuracy of our solver we perform a self-consistent convergence study on the far field pattern. The error is obtained by comparing with the result obtained using 20 panels with $k_0 = 10$ and $k_1 = 5$, and is measured in the L^2 norm. Figure 5a shows that the far field converges exponentially fast when the number of panels increases by 2; we scanned through discretizations with 4 panels to 18 panels.

6.2 Example 2: Scattering from a Rotated Starfish

For the second example, we consider an axisymmetric object with generating curve

$$\begin{aligned} r(t) &= [2 + 0.5 \cos(5\pi(t - 1))] \cos(\pi(t - 0.5)), \\ z(t) &= [2 + 0.5 \cos(5\pi(t - 1))] \sin(\pi(t - 0.5)), \end{aligned} \tag{6.6}$$

for $t \in [0, 1]$. We refer to this object as the rotated *starfish*, as shown in Figure 3. As before, the accuracy of the integral equation solver was tested in this geometry using the extinction theorem (described in Section 6) with known boundary data and fields given in equation (6.1). The accuracy of the solver was verified at several wavenumbers, and results are shown in Table 1b.

Although the generating curve γ is open (when viewed as $\gamma \subset \mathbb{R}^2$), the object is globally smooth. We therefore apply a uniform panel discretization in the parameter space $[0, 1]$.

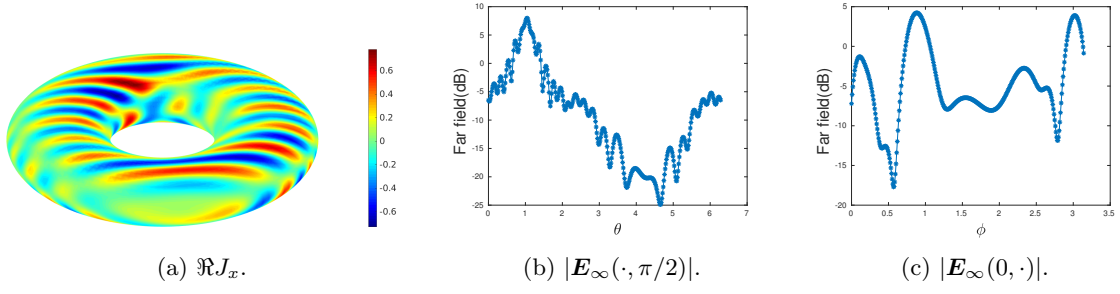


Figure 2: A penetrable torus with interior $k_1 = 5.0$ and background $k_0 = 10.0$.

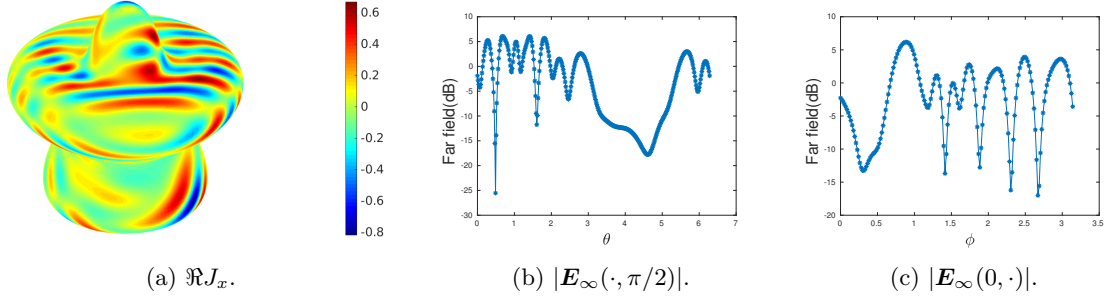


Figure 3: A penetrable star-fish Ω with interior $k_1 = 5.0$ and background $k_0 = 10.0$.

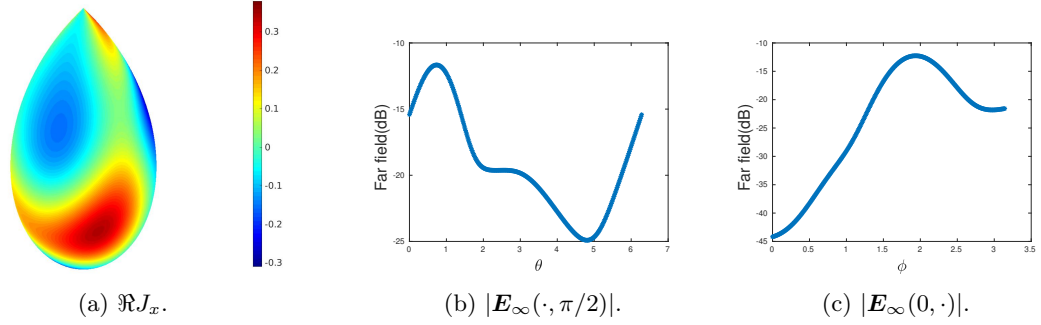


Figure 4: A penetrable droplet Ω with interior $k_1 = 5.0$ and background $k_0 = 10.0$.

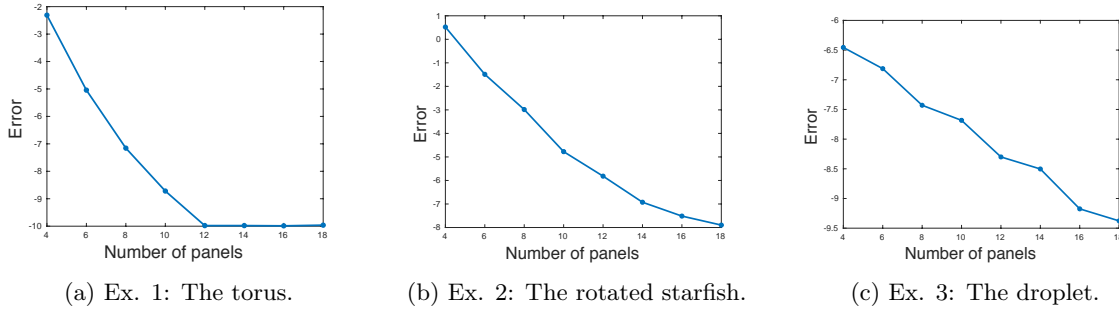


Figure 5: A self-consistent convergence study on the far field pattern of three geometries with interior $k_1 = 5.0$ and background $k_0 = 10.0$. The error of the far field is given on a \log_{10} -scale.

Table 1b provides the accuracy results at various wavenumbers and discretization refinements. We easily obtain 8 to 9 digits of accuracy by using a sufficient number of discretization points per wavelength. The computational time is again dominated by the matrix generation. Once the matrix is generated and factored, the time for additional solves is negligible.

Figure 3 shows the scattering behavior for an incident plane wave with $k_1 = 5$ and $k_0 = 10$. The far field pattern oscillates around $\theta = \pi/3$. This effect is a combination of specular reflection and the changing convexity of the geometry. The far field is notably small near $\theta = 4\pi/3$; this location is in the shadow region with respect to the direction of the incident wave. Again, to verify the accuracy of our solver, Figure 5b provides the results of a self-consistent convergence test of the far field pattern. We obtain exponential convergence when the number of panels is increased by 2, as before.

6.3 Example 3: Scattering from a Droplet

In this example, we consider scattering from a droplet whose generating curve is parameterized as:

$$\begin{aligned} r(t) &= \sin(\pi t) \cos[0.5\pi(t - 1.5)], \\ z(t) &= \sin(\pi t) \sin[0.5\pi(t - 1.5)] + 0.5, \end{aligned} \quad (6.7)$$

for $t \in [0.5, 1]$. As is clear in Figure 4, there is a point singularity at $t = 1$ on the z -axis. To resolve this singularity, we first compute a uniform length panel discretization in the parameter space $[0.5, 1]$. Five dyadic refinements are then performed along the panel adjacent to the end point, yielding a graded mesh. As illustrated in Figure 6a, the last panel near the end point is of size $8.18\text{E-}3$ when $k_1 = 5$ and $k_0 = 10$.

Once again, the accuracy of the integral equation solver was tested in this geometry using the extinction theorem (described in Section 6) with known boundary data and fields given in equation (6.1). The accuracy of the solver was verified at several wavenumbers, and results are shown in Table 1c. More than 8 digits of accuracy was obtained in the tests at various wavenumbers, which implies that the solution to the integral equation near the point singularity of the droplet is also resolved to this accuracy.

Figure 4 then illustrates scattering of an incident plane wave for $k_1 = 5$ and $k_0 = 10$. Unlike the previous two examples, the far field pattern at $\varphi = \pi/2$ and $\theta = 0$ are quite smooth due to the particular geometry and observation angle. However, the far field pattern reaches a minimum near $\theta = 4\pi/3$ due to the specular reflection. Similarly, as before, self-consistent convergence results on the far field pattern are reported in Figure 5c. The plot

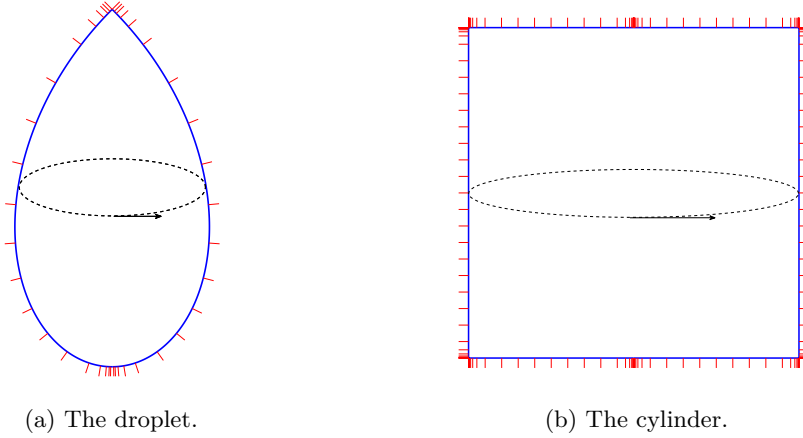


Figure 6: The dyadic refinement on the generating curves for non-smooth geometries.

demonstrates exponential convergence when the number of panels is increased by 2, starting at 4 panels.

6.4 Example 4: Scattering from a Cylinder

Finally, we consider scattering from a cylindrical geometry whose generating curve has vertices given by

$$V = \{(0, -1), (1, -1), (1, 1), (0, 1)\}, \quad (6.8)$$

see Figure 8. Once again, the generating curve is open but gives rise to a smooth surface when crossing the z -axis. However, the cylinder contains an edge at the top and bottom which necessitates dyadic refinement to ensure accuracy. In particular, on the two panels that are adjacent to the corner, dyadic refinement is performed such that the size of the last panel is on the order of $1\text{E-}5$, as illustrated in Figure 6b. This is of course deep sub-wavelength, and is small enough to resolve the solution to the integral equation to sufficiently high accuracy.

The accuracy of the integral equation solver was again tested in this geometry using the extinction theorem (described in Section 6) with known boundary data and fields given in equation (6.1). The accuracy of the solver was verified at several wavenumbers, and results are shown in Table 1d. At small wavenumbers, we obtain approximately 8 digits of accuracy; this accuracy slowly deteriorates as the wavenumber increases. This is due to a stronger singularity near the corner at higher wavenumbers (since the characteristic length-scale of the singularity is on the order of the wavelength). More digits can be obtained if additional refinement were implemented.

For an incident plane wave with $k_0 = 10.0$ and $k_1 = 5.0$, Figure 8 plots the real-part of the x -component of $\mathbf{n} \times \mathbf{H}^{\text{tot}}$ and the far field pattern. At $\varphi = 0$ in the far field pattern, we again see strong and weak scattering near $\theta = \pi/3$ and $\theta = 4\pi/3$, respectively. This effect is due to similar reasons as in the previous three examples.

To demonstrate the accuracy of our solver for scattering from the cylinder, Figure 7a shows the convergence of the electric and magnetic currents when the number of panels is increased by 6, starting with 24 panels. In this case, we have set $k_0 = \pi$, $k_1 = 2\pi$, and the incident plane wave has parameters $\theta_1 = \pi/3$, $\varphi_1 = 2\pi/3$, $\theta_2 = \pi/3$ and $\varphi_2 = \pi/2$ (as in (6.3)). The error is measured in the L^2 norm and is obtained by comparing the results with

Table 1: Accuracy results for scattering from objects in Figures 2-8.

(a) The torus.

| k_0 | k_1 | N_f | N_{pts} | T_{kernel} | T_{matgen} | T_{solve} | T_{add} | E_{error} |
|-------|-------|-------|-----------|--------------|--------------|-------------|-----------|-------------|
| 1 | 2 | 13 | 64 | 2.76E+0 | 2.98E+0 | 6.48E-2 | 1.08E-2 | 2.32E-9 |
| 1 | 5 | 16 | 160 | 6.09E+0 | 7.95E+0 | 3.29E-1 | 2.64E-2 | 4.61E-9 |
| 1 | 10 | 21 | 320 | 1.28E+1 | 2.51E+1 | 3.37E+0 | 8.59E-2 | 3.11E-8 |
| 5 | 2 | 13 | 160 | 6.13E+0 | 7.65E+0 | 3.56E-1 | 3.24E-2 | 1.01E-9 |
| 5 | 10 | 21 | 320 | 1.27E+1 | 2.49E+1 | 2.35E+0 | 8.59E-2 | 3.84E-9 |
| 5 | 20 | 30 | 640 | 6.12E+1 | 1.38E+2 | 2.53E+1 | 5.85E-1 | 4.63E-9 |
| 10 | 5 | 17 | 320 | 1.32E+1 | 2.36E+1 | 1.97E+0 | 6.99E-2 | 1.61E-9 |
| 10 | 20 | 30 | 640 | 6.14E+1 | 1.37E+2 | 2.49E+1 | 5.36E-1 | 2.08E-9 |
| 10 | 40 | 45 | 640 | 9.14E+1 | 2.06E+2 | 3.49E+1 | 8.37E-1 | 2.66E-8 |
| 20 | 5 | 17 | 320 | 1.76E+1 | 2.77E+1 | 2.95E+0 | 9.8E-2 | 4.78E-9 |
| 20 | 10 | 22 | 640 | 6.09E+1 | 1.17E+2 | 1.83E+1 | 4.14E-1 | 3.37E-9 |
| 20 | 40 | 45 | 640 | 9.64E+1 | 2.11E+2 | 3.30E+1 | 8.37E-1 | 1.10E-8 |

(b) The rotated starfish.

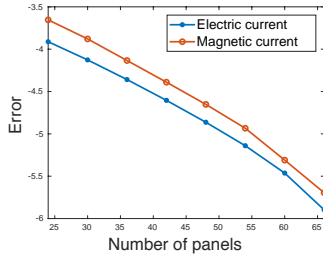
| k_0 | k_1 | N_f | N_{pts} | T_{kernel} | T_{matgen} | T_{solve} | T_{add} | E_{error} |
|-------|-------|-------|-----------|--------------|--------------|-------------|-----------|-------------|
| 5 | 2 | 10 | 224 | 6.47E+0 | 9.34E+0 | 4.61E-1 | 3.35E-2 | 1.24E-9 |
| 5 | 10 | 16 | 304 | 9.49E+0 | 1.80E+1 | 1.57E+0 | 6.59E-2 | 3.44E-10 |
| 5 | 20 | 21 | 464 | 2.96E+1 | 6.19E+1 | 7.01E+0 | 2.06E-1 | 1.51E-9 |
| 10 | 5 | 13 | 304 | 9.82E+0 | 1.69E+1 | 1.78E+0 | 6.48E-2 | 2.04E-10 |
| 10 | 20 | 21 | 464 | 3.01E+1 | 5.94E+1 | 7.21E+0 | 2.59E-1 | 9.74E-10 |
| 10 | 40 | 30 | 784 | 7.73E+1 | 2.09E+2 | 3.98E+1 | 7.31E-1 | 1.45E-8 |
| 20 | 5 | 13 | 464 | 2.90E+1 | 4.93E+1 | 1.97E+1 | 6.99E-1 | 1.05E-10 |
| 20 | 10 | 16 | 464 | 2.98E+1 | 5.50E+1 | 7.78E+1 | 1.84E-1 | 4.41E-10 |
| 20 | 40 | 30 | 784 | 7.85E+1 | 2.17E+2 | 4.02E+1 | 8.04E-1 | 4.60E-9 |
| 40 | 5 | 13 | 784 | 7.41E+1 | 1.39E+2 | 2.02E+1 | 3.34E-1 | 3.39E-10 |
| 40 | 10 | 16 | 784 | 7.56E+1 | 1.55E+2 | 2.58E+1 | 4.46E-1 | 3.58E-9 |
| 40 | 20 | 21 | 784 | 7.75E+1 | 1.73E+2 | 3.32E+1 | 5.01E-1 | 3.01E-9 |

(c) The droplet.

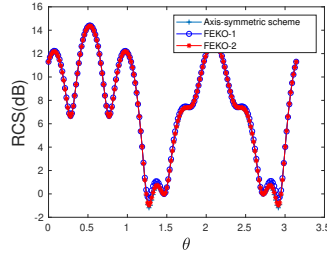
| k_0 | k_1 | N_f | N_{pts} | T_{kernel} | T_{matgen} | T_{solve} | T_{add} | E_{error} |
|-------|-------|-------|-----------|--------------|--------------|-------------|-----------|-------------|
| 5 | 2 | 7 | 224 | 1.67E+1 | 1.89E+1 | 3.24E-1 | 6.01E-2 | 2.71E-10 |
| 5 | 10 | 10 | 320 | 3.05E+1 | 3.72E+1 | 7.14E-1 | 8.39E-2 | 1.86E-9 |
| 5 | 20 | 11 | 480 | 7.52E+1 | 9.43E+1 | 2.39E+0 | 1.84E-1 | 5.11E-9 |
| 10 | 5 | 9 | 320 | 3.05E+1 | 3.67E+1 | 5.47E-1 | 7.59E-2 | 1.24E-10 |
| 10 | 20 | 11 | 480 | 7.80E+1 | 9.69E+1 | 2.45E+0 | 1.84E-1 | 2.59E-9 |
| 10 | 40 | 14 | 800 | 2.02E+2 | 2.79E+2 | 1.13E+1 | 9.27E-1 | 6.76E-9 |
| 20 | 5 | 9 | 480 | 7.27E+1 | 8.86E+1 | 1.97E+0 | 2.28E-1 | 5.81E-10 |
| 20 | 10 | 10 | 480 | 7.56E+1 | 9.34E+1 | 1.99E+0 | 2.52E-1 | 1.31E-10 |
| 20 | 40 | 14 | 800 | 2.04E+2 | 2.77E+2 | 1.12E+1 | 9.27E-1 | 3.43E-9 |
| 40 | 5 | 9 | 800 | 1.89E+2 | 2.39E+2 | 7.77E+0 | 6.07E-1 | 3.48E-10 |
| 40 | 10 | 10 | 800 | 1.92E+2 | 2.53E+2 | 8.19E+0 | 5.88E-1 | 6.12E-10 |
| 40 | 20 | 12 | 800 | 2.05E+2 | 2.66E+2 | 1.01E+1 | 8.01E-1 | 1.45E-10 |

(d) The cylinder.

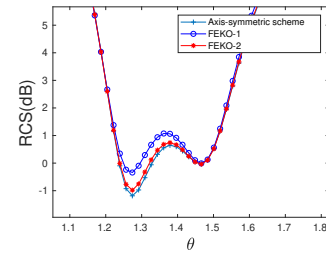
| k_0 | k_1 | N_f | N_{pts} | T_{kernel} | T_{matgen} | T_{solve} | T_{add} | E_{error} |
|-------|-------|-------|-----------|--------------|--------------|-------------|-----------|-------------|
| 2 | 1 | 9 | 1312 | 1.06E+2 | 2.66E+2 | 4.46E+1 | 5.31E-1 | 4.11E-9 |
| 2 | 5 | 11 | 1440 | 1.56E+2 | 3.80E+2 | 7.13E+1 | 7.26E-1 | 2.56E-8 |
| 2 | 10 | 14 | 1696 | 2.18E+2 | 7.97E+2 | 1.35E+2 | 1.31E0 | 9.32E-7 |
| 5 | 2 | 10 | 1440 | 1.41E+2 | 3.58E+2 | 6.56E+1 | 6.63E-1 | 1.54E-8 |
| 5 | 10 | 14 | 1696 | 2.21E+2 | 7.17E+2 | 1.34E+2 | 1.42E0 | 5.92E-8 |
| 5 | 20 | 17 | 2208 | 3.44E+2 | 3.14E+3 | 3.61E+2 | 2.61E0 | 9.74E-7 |
| 10 | 2 | 10 | 1696 | 1.94E+2 | 5.64E+2 | 9.92E+1 | 9.15E-1 | 1.91E-8 |
| 10 | 5 | 11 | 1696 | 2.21E+2 | 5.99E+2 | 1.07E+2 | 1.03E0 | 3.95E-8 |
| 10 | 20 | 17 | 2208 | 3.49E+2 | 2.27E+3 | 3.62E+2 | 2.54E0 | 2.24E-6 |
| 20 | 2 | 10 | 2208 | 3.29E+2 | 1.15E+3 | 2.19E+2 | 1.51E0 | 3.54E-8 |
| 20 | 5 | 11 | 2208 | 3.41E+2 | 1.23E+3 | 2.38E+2 | 1.61E0 | 1.39E-7 |
| 20 | 10 | 14 | 2208 | 3.43E+2 | 1.49E+3 | 2.96E+2 | 2.08E0 | 1.32E-7 |



(a) Current error



(b) $|\mathbf{E}_\infty(\cdot, \pi/2)|^2$



(c) A zoom in of $|\mathbf{E}_\infty(\cdot, \pi/2)|^2$

Figure 7: Validating convergence results for the cylinder. (a) Self-consistent convergence of the electric and magnetic current from the scattering of a penetrable cylinder when the number of discretization panels is increased. The error is given in the logarithmic scale. (b) A comparison of the radar cross section computed using our scheme and that obtained by *FEKO*. Lines labeled *FEKO-1* were obtained from a coarse mesh (edge length 0.2) and lines labeled *FEKO-2* were obtained using a fine mesh (edge length 0.1). (c) A blow-up of part of results in (b).

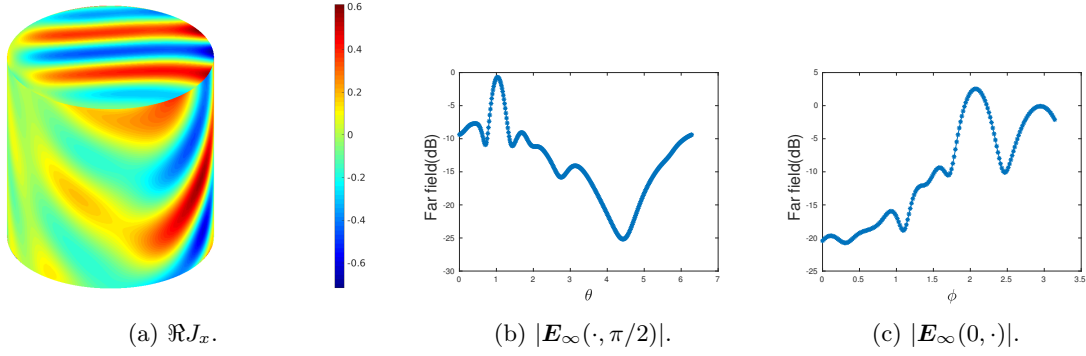


Figure 8: A penetrable cylinder Ω with interior $k_1 = 5.0$ and background $k_0 = 10.0$.

those obtained using a 72 panel discretization. To further validate the numerical results of our solver we compare our far-field patterns with those computed using the commercial software package *FEKO*, which also uses a boundary integral method (i.e. method of moments). Figure 7b and 7c show a comparison of the radar cross section (RCS) of the cylinder when $\varphi = \pi/2$ and $\theta \in [0, 2\pi]$ (the RCS is the square of the modulus of the far-field pattern). Two different meshes are used to compute the RCS in *FEKO*. One is on a coarse mesh with edge length 0.2 and another one is on a refined mesh with edge length 0.1. It can be seen from Figure 7 that the results from *FEKO* converge to the result obtained by our scheme. It should be also noticed that our solvers used to obtain the results in Figures 7b and 7c only requires 18 seconds for 37 modes and 24 panels (i.e. 384 discretization points on the generating curve); since *FEKO* does not take advantage of axisymmetric geometry, and does not discretize to high-order, more than 200 seconds were required to obtain the solution on the refined mesh (edge length 0.1).

7 Conclusion

In this paper, we provided a derivation of Müller’s integral equation, and its indirect formulation, for electromagnetic scattering from piecewise constant penetrable media. The resulting integral equations are second-kind when the boundary of the inclusion is smooth, and remain relatively well-conditioned on L^2 when the boundary has a modest number of edges or geometric singularities. In either case, the integral equation representation admits a unique solution for all ranges of interior and exterior material properties (as defined in the introduction). Our numerical solver strongly takes advantage of the axisymmetric geometry by using a Fourier-based separation of variables in the azimuthal angle to obtain a sequence of decoupled integral equations along a cross section of the geometry. Using FFTs, discrete convolution, kernel splitting, and novel recurrence relations we are able to efficiently evaluate the modal Green’s functions and their derivatives. High-order accurate convergence is observed when discretizing the integral equations using generalized Gaussian quadratures and an adaptive Nyström-like method. Numerical examples show that the algorithm can efficiently and accurately solve the scattering problem from various axisymmetric objects, even in the presence of geometric edge and point singularities.

Throughout all the numerical examples, we assume the frequency ω is in the resonant regime. In particular, it is not close to zero. In the low-frequency regime, when ω approaches

zero, the operator $\mathcal{K}^k/(i\omega)$ becomes numerically unstable, which leads to the well-known low-frequency breakdown issue [18–20]. In that case, Müller’s formulation (as well as its indirect form) has to be modified to overcome this instability. Some helpful discussions regarding this can be found in [36]. However, when ω is not close to zero, the integral equation formulations of this paper extend directly and remain well-conditioned in more complicated geometries. Extensions to arbitrary geometries in three dimensions are underway, but will of course require a completely new set of tools (fast algorithms, quadrature, etc.). We will report on this in the future.

A Proof of the recursion formulas

For simplicity, we consider

$$\mathcal{P}_m = \int_0^{2\pi} \frac{\cos m\varphi}{\sqrt{\chi - \cos \varphi}} d\varphi \quad (\text{A.1})$$

instead of $\mathcal{Q}_{m-1/2}(\chi)$, since $\mathcal{Q}_{m-1/2}(\chi) = \mathcal{P}_m/\sqrt{8}$, and

$$\mathcal{S}_m(\chi) = \int_0^{2\pi} \frac{\cos m\varphi}{(\chi - \cos \varphi)^{3/2}} d\varphi, \quad (\text{A.2})$$

$$\mathcal{T}_m(\chi) = \int_0^{2\pi} \frac{\cos m\varphi}{\chi - \cos \varphi} d\varphi. \quad (\text{A.3})$$

We first derive the recursion formula for \mathcal{P}_m .

Lemma A.1 *If $m \geq 1$, then*

$$\mathcal{P}_{m+1}(\chi) = \frac{4m}{2m+1} \chi \mathcal{P}_m(\chi) - \frac{2m-1}{2m+1} \mathcal{P}_{m-1}(\chi). \quad (\text{A.4})$$

Proof Starting from \mathcal{P}_{m+1}

$$\begin{aligned} \mathcal{P}_{m+1}(\chi) &= \int_0^{2\pi} \frac{\cos(m+1)\varphi}{\sqrt{\chi - \cos \varphi}} d\varphi \\ &= \int_0^{2\pi} \frac{\cos(m-1)\varphi}{\sqrt{\chi - \cos \varphi}} d\varphi - 2 \int_0^{2\pi} \frac{\sin \varphi \sin m\varphi}{\sqrt{\chi - \cos \varphi}} d\varphi \\ &= \int_0^{2\pi} \frac{\cos(m-1)\varphi}{\sqrt{\chi - \cos \varphi}} d\varphi - 4 \int_0^{2\pi} \sin m\varphi d(\sqrt{\chi - \cos \varphi}) \\ &= \int_0^{2\pi} \frac{\cos(m-1)\varphi}{\sqrt{\chi - \cos \varphi}} d\varphi + 4m \int_0^{2\pi} \cos m\varphi \sqrt{\chi - \cos \varphi} d\varphi \\ &= \mathcal{P}_{m-1}(\chi) + 4m \mathcal{O}_m(\chi), \end{aligned} \quad (\text{A.5})$$

where

$$\mathcal{O}_m(\chi) = \int_0^{2\pi} \cos m\varphi \sqrt{\chi - \cos \varphi} d\varphi, \quad (\text{A.6})$$

and also by noting that \mathcal{P}_m can be expanded as:

$$\begin{aligned}
\mathcal{P}_m &= \int_0^{2\pi} \frac{\cos m\varphi}{\sqrt{\chi - \cos \varphi}} d\varphi \\
&= \frac{1}{\chi} \int_0^{2\pi} \frac{(\chi - \cos \varphi) \cos m\varphi}{\sqrt{\chi - \cos \varphi}} d\varphi + \frac{1}{\chi} \int_0^{2\pi} \frac{\cos \varphi \cos m\varphi}{\sqrt{\chi - \cos \varphi}} d\varphi \\
&= \frac{1}{\chi} \mathcal{O}_m(\chi) + \frac{1}{\chi} \left(\int_0^{2\pi} \frac{\cos(m-1)\varphi}{\sqrt{\chi - \cos \varphi}} d\varphi - \int_0^{2\pi} \frac{\sin \varphi \sin m\varphi}{\sqrt{\chi - \cos \varphi}} d\varphi \right) \\
&= \frac{1}{\chi} \mathcal{O}_m(\chi) + \frac{1}{\chi} (\mathcal{P}_{m-1}(\chi) + 2m \mathcal{O}_m(\chi)).
\end{aligned} \tag{A.7}$$

The recursion formula follows by combining the two expressions together. \square

Lemma A.2 *If $m \geq 1$, then*

$$\mathcal{S}_m(\chi) = \frac{(1-2m)\chi \mathcal{P}_m(\chi) - (1-2m) \mathcal{P}_{m-1}(\chi)}{\chi^2 - 1}. \tag{A.8}$$

Proof Performing a similar calculation as in the previous lemma, we have:

$$\begin{aligned}
\mathcal{S}_m(\chi) &= \frac{1}{\chi} \int_0^{2\pi} \frac{(\chi - \cos \varphi) \cos m\varphi}{(\chi - \cos \varphi)^{3/2}} d\varphi + \frac{1}{\chi} \int_0^{2\pi} \frac{\cos \varphi \cos m\varphi}{(\chi - \cos \varphi)^{3/2}} d\varphi \\
&= \frac{1}{\chi} \mathcal{P}_m(\chi) + \frac{1}{\chi} \mathcal{U}_m(\chi),
\end{aligned} \tag{A.9}$$

where

$$\mathcal{U}_m(\chi) = \int_0^{2\pi} \frac{\cos \varphi \cos m\varphi}{(\chi - \cos \varphi)^{3/2}} d\varphi. \tag{A.10}$$

It then holds that

$$\begin{aligned}
\mathcal{U}_m(\chi) &= \frac{1}{\chi} \int_0^{2\pi} \frac{(\chi \cos \varphi - \cos^2 \varphi) \cos m\varphi}{(\chi - \cos \varphi)^{3/2}} d\varphi + \frac{1}{\chi} \int_0^{2\pi} \frac{\cos^2 \varphi \cos m\varphi}{(\chi - \cos \varphi)^{3/2}} d\varphi \\
&= \frac{1}{\chi} \int_0^{2\pi} \frac{\cos \varphi \cos m\varphi}{(\chi - \cos \varphi)^{1/2}} d\varphi + \frac{1}{\chi} \int_0^{2\pi} \frac{\cos^2 \varphi \cos m\varphi}{(\chi - \cos \varphi)^{3/2}} d\varphi \\
&= \frac{1}{2\chi} (\mathcal{P}_{m+1}(\chi) + \mathcal{P}_{m-1}(\chi)) + \frac{1}{\chi} \left(\int_0^{2\pi} \frac{\cos m\varphi}{(\chi - \cos \varphi)^{3/2}} d\varphi - \int_0^{2\pi} \frac{\sin^2 \varphi \cos m\varphi}{(\chi - \cos \varphi)^{3/2}} d\varphi \right) \\
&= \frac{1}{2\chi} (\mathcal{P}_{m+1}(\chi) + \mathcal{P}_{m-1}(\chi)) + \frac{1}{\chi} \mathcal{S}_m(\chi) + \frac{2}{\chi} \int_0^{2\pi} \sin \varphi \cos m\varphi d \left(\frac{1}{\sqrt{\chi - \cos \varphi}} \right) \\
&= \frac{1}{2\chi} (\mathcal{P}_{m+1}(\chi) + \mathcal{P}_{m-1}(\chi)) + \frac{1}{\chi} \mathcal{S}_m(\chi) - \frac{2}{\chi} \int_0^{2\pi} \frac{\cos \varphi \cos m\varphi}{\sqrt{\chi - \cos \varphi}} d\varphi + \frac{2m}{\chi} \int_0^{2\pi} \frac{\sin \varphi \sin m\varphi}{\sqrt{\chi - \cos \varphi}} d\varphi \\
&= \frac{1}{2\chi} (\mathcal{P}_{m+1}(\chi) + \mathcal{P}_{m-1}(\chi)) + \frac{1}{\chi} \mathcal{S}_m(\chi) - \frac{1}{\chi} (\mathcal{P}_{m+1}(\chi) + \mathcal{P}_{m-1}(\chi)) - \frac{m}{\chi} (\mathcal{P}_{m+1}(\chi) - \mathcal{P}_{m-1}(\chi)).
\end{aligned} \tag{A.11}$$

Combining equations (A.9) and (A.11), and using Lemma A.1, we obtain the final recurrence relation

$$\begin{aligned}
\mathcal{S}_m(\chi) &= \frac{1}{\chi^2 - 1} \left(\chi \mathcal{P}_m(\chi) + \frac{2m-1}{2} \mathcal{P}_{m-1}(\chi) - \frac{2m+1}{2} \mathcal{P}_{m+1}(\chi) \right) \\
&= \frac{1}{\chi^2 - 1} ((1-2m)\chi \mathcal{P}_m(\chi) - (1-2m) \mathcal{P}_{m-1}(\chi)).
\end{aligned} \tag{A.12}$$

This ends the proof. \square

Finally, we have the following lemma and its proof.

Lemma A.3 *If $m \geq 1$, then $\mathcal{T}_{m+1}(\chi) = 2\chi\mathcal{T}_m(\chi) - \mathcal{T}_{m-1}(\chi)$.*

Proof

$$\begin{aligned}\mathcal{T}_m(\chi) &= \frac{1}{\chi} \int_0^{2\pi} \frac{\chi \cos m\varphi}{\chi - \cos \varphi} d\varphi \\ &= \frac{1}{\chi} \int_0^{2\pi} \frac{\cos \varphi \cos m\varphi}{\chi - \cos \varphi} d\varphi \\ &= \frac{1}{2\chi} (\mathcal{T}_{m+1}(\chi) + \mathcal{T}_{m-1}(\chi)).\end{aligned}\tag{A.13}$$

References

- [1] B. Alpert. Hybrid Gauss-trapezoidal quadrature rules. *SIAM J. Sci. Comput.*, 20(5):1551–1584, 1999.
- [2] M. Andreasen. Scattering from bodies of revolution. *IEEE Trans. Antennas Propag.*, 13(2):303–310, 1965.
- [3] P. K. Banerjee and R. Butterfield. *Boundary element methods in engineering science*. McGraw-Hill, London, UK, 1981.
- [4] J. Bremer. On the Nyström discretization of integral equations on planar curves with corners. *Appl. Comput. Harm. Anal.*, 32:45–64, 2012.
- [5] J. Bremer and Z. Gimbutas. A Nyström method for weakly singular integral operators on surfaces. *J. Comput. Phys.*, 231(14):4885–4903, 2012.
- [6] J. Bremer, Z. Gimbutas, and V. Rokhlin. A nonlinear optimization procedure for generalized Gaussian quadratures. *SIAM J. Sci. Comput.*, 32(4):1761–1788, 2010.
- [7] W. L. Briggs and V. E. Henson. *The DFT: An Owner’s Manual for the Discrete Fourier Transform*. SIAM, Philadelphia, PA, 1995.
- [8] O. P. Bruno. Fast, high-order, high-frequency integral methods for computational acoustics and electromagnetics. In *Topics in computational wave propagation*, pages 43–82. Springer, 2003.
- [9] O. P. Bruno, T. Elling, R. Paffenroth, and C. Turc. Electromagnetic integral equations requiring small numbers of Krylov-subspace iterations. *J. Comput. Phys.*, 228:6169–6183, 2009.
- [10] O. P. Bruno and F. Reitich. Boundary-variation solutions for bounded-obstacle scattering problems in three dimensions. *J. Acoust. Soc. Am.*, 104(5):2579–2583, 1998.
- [11] V. S. Bulygin, T. M. Benson, Y. V. Gandel, and A. I. Nosich. Full-Wave Analysis and Optimization of a TARA-Like Shield-Assisted Paraboloidal Reflector Antenna Using a Nystrom-Type Method. *IEEE Trans. Antennas Propag.*, 61(10):4981–4989, 2013.

- [12] W. C. Chew, M. S. Tong, and B. Hu. *Integral Equation Methods for Electromagnetic and Elastic Waves*. Morgan & Claypool, Williston, VT, USA, 2009.
- [13] H. S. Cohl and J. E. Tohline. A compact cylindrical Green’s function expansion for the solution of potential problems. *Astrophys. J.*, 527(1):86–101, 1999.
- [14] D. Colton and R. Kress. *Integral Equation Method in Scattering Theory*. Wiley-Interscience, New York, 1983.
- [15] J. T. Conway and H. S. Cohl. Exact Fourier expansion in cylindrical coordinates for the three-dimensional Helmholtz Green function. *Z. Angew. Math. Phys.*, 61:425–442, 2010.
- [16] M. Costabel. Boundary integral operators on lipschitz domains: Elementary results. *SIAM J. Math. Anal.*, 19:613–626, 1988.
- [17] E. A. Dunn, J.-K. Byun, E. D. Branch, and J.-M. Jin. Numerical Simulation of BOR Scattering and Radiation Using a Higher Order FEM. *IEEE Trans. Antennas Propag.*, 54(3):945–952, 2006.
- [18] C. L. Epstein and L. Greengard. Debye Sources and the Numerical Solution of the Time Harmonic Maxwell Equations. *Comm. Pure Appl. Math.*, 63(4):413–463, 2010.
- [19] C. L. Epstein, L. Greengard, and M. O’Neil. Debye Sources and the Numerical Solution of the Time Harmonic Maxwell Equations II. *Comm. Pure Appl. Math.*, 66(5):753–789, 2013.
- [20] C. L. Epstein, L. Greengard, and M. O’Neil. A high-order wideband direct solver for electromagnetic scattering from bodies of revolution. *J. Comput. Phys.*, 2019. To appear.
- [21] Q. Fang, D. P. Nicholls, and J. Shen. A stable, high-order method for three-dimensional, bounded obstacle, acoustic scattering. *J. Comput. Phys.*, 224(2):1145–1169, 2007.
- [22] J. L. Fleming, A. W. Wood, and W. D. W. Jr. Locally corrected Nyström method for EM scattering by bodies of revolution. *J. Comput. Phys.*, 196:41–52, 2004.
- [23] S. D. Gedney and R. Mittra. The use of the FFT for the efficient solution of the problem of electromagnetic scattering by a body of revolution. *IEEE Trans. Antennas Propag.*, 38:313–322, 1990.
- [24] N. Geng and L. Carin. Wide-band electromagnetic scattering from a dielectric BOR buried in a layered lossy dispersive medium. *IEEE Trans. Antennas Propag.*, 47(4):610–619, 1999.
- [25] A. Gil, J. Segura, and N. M. Temme. *Numerical Methods for Special Functions*. SIAM, Philadelphia, PA, 2007.
- [26] A. Gillman, P. M. Young, and P.-G. Martinsson. A direct solver with $O(N)$ complexity for integral equations on one-dimensional domains. *Front. Math. China*, 7(2):217–247, 2012.

- [27] Z. Gimbutas and L. Greengard. Fast multi-particle scattering: A hybrid solver for the Maxwell equations in microstructured materials. *J. Comput. Phys.*, 232:22–32, 2013.
- [28] M. Gustafsson. Accurate and efficient evaluation of modal Green’s functions. *J. Electromagnet. Wave.*, 24(10):1291–1301, 2010.
- [29] S. Hao, A. H. Barnett, P. G. Martinsson, and P. Young. High-order accurate Nyström discretization of integral equations with weakly singular kernels on smooth curves in the plane. *Adv. Comput. Math.*, 40:245–272, 2014.
- [30] S. Hao, P.-G. Martinsson, and P. Young. An efficient and highly accurate solver for multi-body acoustic scattering problems involving rotationally symmetric scatterers. *Comput. Math. Appl.*, 69:304–318, 2015.
- [31] R. F. Harrington. *Field Computation by Moment Methods*. Macmillan, Co., New York, NY, 1968.
- [32] J. Helsing and A. Holst. Variants of an explicit kernel-split panel-based Nyström discretization scheme for Helmholtz boundary value problems. *Adv. Comput. Math.*, 41:691–708, 2015.
- [33] J. Helsing and A. Karlsson. An explicit kernel-split panel-based Nyström scheme for integral equations on axially symmetric surfaces. *J. Comput. Phys.*, 272:686–703, 2014.
- [34] J. Helsing and A. Karlsson. Determination of Normalized Magnetic Eigenfields in Microwave Cavities. *IEEE Trans. Microw. Theory Tech.*, 63(5):1457–1467, 2015.
- [35] J. Helsing and A. Karlsson. Determination of normalized electric eigenfields in microwave cavities with sharp edges. *J. Comput. Phys.*, 304:465 – 486, 2016.
- [36] J. Helsing and A. Karlsson. Resonances in axially symmetric dielectric objects. *IEEE Trans. Microw. Theory Tech.*, 65(7):2214–2227, 2017.
- [37] K. L. Ho and L. Greengard. A fast direct solver for structured linear systems by recursive skeletonization. *SIAM J. Sci. Comput.*, 34(5):2507–2532, 2012.
- [38] L.-M. Imbert-Gerard, F. Vico, L. Greengard, and M. Ferrando. Integral equation methods for electrostatics, acoustics and electromagnetics in smoothly varying, anisotropic media. 2018. arXiv:1805.04791 [math.NA].
- [39] J. D. Jackson. *Classical Electrodynamics*. Wiley, Hoboken, NJ, 3rd edition, 1999.
- [40] A. Kirsch and F. Hettlich. *The Mathematical Theory of Time-Harmonic Maxwell’s Equations*. Springer Verlag, Cham, Switzerland, 2015.
- [41] R. Kress. *Linear Integral Equations*. Springer, New York, 1999.
- [42] J. Lai, S. Ambikasaran, and L. F. Greengard. A Fast Direct Solver for High Frequency Scattering from a Large Cavity in Two Dimensions. *SIAM J. Sci. Comput.*, 36(6):B887–B903, 2014.

- [43] J. Lai, L. Greengard, and M. O’Neil. Robust integral formulations for electromagnetic scattering from three-dimensional cavities. *Journal of Computational Physics*, 345:1 – 16, 2017.
- [44] Y. Liu and A. H. Barnett. Efficient numerical solution of acoustic scattering from doubly-periodic arrays of axisymmetric objects. *J. Comput. Phys.*, 324:226 – 245, 2016.
- [45] J. R. Mautz and R. F. Harrington. Radiation and scattering from bodies of revolution. *Appl. Sci. Res.*, 20(1):405–435, 1969.
- [46] J. R. Mautz and R. F. Harrington. Electromagnetic scattering from a homogeneous body of revolution. Technical report, Department of Electrical and Computer Engineering, Syracuse, NY, November 1977. TS-77-20.
- [47] J. R. Mautz and R. F. Harrington. H-field, E-field and combined-field solutions for conducting bodies of revolution. *Arch. Elec. Übertragung.*, 32:159–164, 1978.
- [48] L. N. Medgyesi-Mitschang and J. M. Putnam. Electromagnetic Scattering from Axially Inhomogeneous Bodies of Revolution. *IEEE Trans. Antennas Propag.*, 32(8):797–806, 1984.
- [49] M. A. Morgan and K. K. Mei. Finite-Element Computation of Scattering by Inhomogeneous Penetrable Bodies of Revolution. *IEEE Trans. Antennas Propag.*, 27(2):202–214, 1979.
- [50] C. Müller. *Foundations of the Mathematical Theory of Electromagnetic Waves*. Springer Verlag, 1969.
- [51] J.-C. Nédélec. *Acoustic and Electromagnetic Equations*. Springer-Verlag New York, 2001.
- [52] D. P. Nicholls and J. Shen. A Stable High-Order Method for Two-Dimensional Bounded-Obstacle Scattering. *SIAM J. Sci. Comput.*, 28(4):1398–1419, 2006.
- [53] F. W. J. Olver, D. W. Lozier, R. F. Boisvert, and C. W. Clark. *NIST Handbook of Mathematical Functions*. Cambridge University Press, New York, 2010.
- [54] M. O’Neil and A. J. Cerfon. An integral equation-based numerical solver for Taylor states in toroidal geometries. *J. Comput. Phys.*, 359:263–282, 2018.
- [55] V. Rokhlin. Solution of acoustic scattering problems by means of second kind integral equations. *Wave Motion*, 5:257–272, 1983.
- [56] Y. Saad and M. Schultz. GMRES: A generalized minimal residual algorithm for solving nonsymmetric linear-systems. *SIAM J. Sci. Stat. Comput.*, 7:856–869, 1986.
- [57] K. Serkh and V. Rokhlin. On the solution of elliptic partial differential equations on regions with corners. *J. Comput. Phys.*, 305:150–171, 2016.
- [58] E. N. Vasil’ev and L. B. materikova. Excitation of Dielectric Bodies of Revolution. *Soviet Physics - Technical Physics*, 10(10):1401–1406, 1966.

- [59] F. Vico, L. Greengard, and M. Ferrando. Decoupled field integral equations for electromagnetic scattering from homogeneous penetrable obstacles. *Commun. Part. Diff. Eq.*, 43(2):159–184, 2018.
- [60] N. Yarvin and V. Rokhlin. Generalized Gaussian Quadratures and Singular Value Decompositions of Integral Operators. *SIAM J. Sci. Comput.*, 20(2):699–718, 1998.
- [61] P. Young, S. Hao, and P. G. Martinsson. A high-order Nyström discretization scheme for boundary integral equations defined on rotationally symmetric surfaces. *J. Comput. Phys.*, 231(11):4142–4159, 2012.
- [62] P. M. Young and P.-G. Martinsson. A Direct Solver for the Rapid Solution of Boundary Integral Equations on Axisymmetric Surfaces in Three Dimensions. 2010. arXiv:1002.2001 [math.NA].
- [63] W. M. Yu, D. G. Fang, and T. J. Cui. Closed Form Modal Green’s Functions for Accelerated Computation of Bodies of Revolution. *IEEE Trans. Antennas Propag.*, 56(11):3452–3461, 2008.